NAVAL POSTGRADUATE SCHOOL
Monterey, California

THESIS

**TRANSIENT LOCALIZATION
IN SHALLOW WATER ENVIRONMENTS
WITH A VERTICAL LINE ARRAY**

by

Gerard Tas

June 2000

Thesis Advisor: Kevin B. Smith
Second Reader: Mitchell Shipley

Approved for public release; distribution is unlimited.

REPORT DOCUMENTATION PAGE

Form Approved OMB No. 0704-0188

1. AGENCY USE ONLY	2. REPORT DATE	3. REPORT TYPE AND DATES COVERED
	June 2000	Master's Thesis

4. TITLE AND SUBTITLE
Transient Localization in Shallow Water Environments with a Vertical Line Array

5. FUNDING NUMBERS

6. AUTHOR Tas, Gerard

7. PERFORMING ORGANIZATION NAME(S) AND ADDRESS(ES)
Naval Postgraduate School
Monterey CA 93943-5000

8. PERFORMING ORGANIZATION REPORT NUMBER

9. SPONSORING/MONITORING AGENCY NAME(S) AND ADDRESS(ES)
Meaningful Color Pages

10. SPONSORING/MONITORING AGENCY REPORT NUMBER

11. SUPPLEMENTARY NOTES The views expressed in this thesis are those of the authors and do not reflect the official policy or position of the Department of Defense or the U.S. Government.

12a. DISTRIBUTION/AVAILABILITY STATEMENT
Approved for public release; distribution is unlimited.

12b. DISTRIBUTION CODE

13. ABSTRACT *(maximum 200 words)*

Several algorithms based on autocorrelation matching of multiple hydrophone elements in a vertical line array have been developed to localize a broadband transient signal. An earlier developed frequency-domain autocorrelation matching (FACM) algorithm was based on autocorrelation matching of only a single hydrophone. The success and robustness of this algorithm in the presence of environmental mismatch was the motivation to adapt it to include the additional information of multiple hydrophones. The new algorithms developed were based on joint autocorrelation matching, specifically depth- and frequency-domain autocorrelation matching (ZFACM), wavenumber- and frequency-domain autocorrelation matching (KzFACM), and an incoherent summation of the FACM results of all the elements in a vertical line array (IFACM). These algorithms were tested in simple, shallow water environments with and without mismatch in the specification of acoustic parameters (e.g., bathymetry and sound speed).

The results suggest that the use of the additional information from multiple elements does improve both the accuracy and robustness of the localizations. All of the algorithms produced similar results, although the IFACM and the KzFACM algorithms appeared to perform slightly better than the ZFACM algorithm in the presence of mismatch. However, the relative performance of the algorithms appeared to be sensitive to the environment and placement of the source and receivers in the waveguide.

14. SUBJECT TERMS	15. NUMBER OF PAGES
Joint autocorrelation matching, Depth- and frequency-domain autocorrelation matching, Wavenumber- and frequency-domain autocorrelation matching	91
	16. PRICE CODE

17. SECURITY CLASSIFICATION OF REPORT	18. SECURITY CLASSIFICATION OF THIS PAGE	19. SECURITY CLASSIFICATION OF ABSTRACT	20. LIMITATION OF ABSTRACT
Unclassified	Unclassified	Unclassified	UL

NSN 7540-01-280-5500

Standard Form 298 (Rev. 2-89)
Prescribed by ANSI Std. 239-18 298-102

Approved for public release; distribution is unlimited.

TRANSIENT LOCALIZATION IN SHALLOW WATER ENVIRONMENTS WITH A VERTICAL LINE ARRAY

Gerard Tas
Lieutenant Commander, Royal Netherlands Navy
Royal Netherlands Naval College, 1985

Submitted in partial fulfillment of the
requirements for the degree of

MASTER OF SCIENCE IN ENGINEERING ACOUSTICS

from the

NAVAL POSTGRADUATE SCHOOL
June 2000

Author: _____
Gerard Tas

Approved by: _____
Kevin B. Smith, Thesis Advisor

_____
Mitchell Shipley, Second Reader

_____
Kevin B. Smith, Chairman
Engineering Acoustics Academic Group

ABSTRACT

Several algorithms based on autocorrelation matching of multiple hydrophone elements in a vertical line array have been developed to localize a broadband transient signal. An earlier developed frequency-domain autocorrelation matching (FACM) algorithm was based on autocorrelation matching of only a single hydrophone. The success and robustness of this algorithm in the presence of environmental mismatch was the motivation to adapt it to include the additional information of multiple hydrophones. The new algorithms developed were based on joint autocorrelation matching, specifically depth- and frequency-domain autocorrelation matching (ZFACM), wavenumber- and frequency-domain autocorrelation matching (KzFACM), and an incoherent summation of the FACM results of all the elements in a vertical line array (IFACM). These algorithms were tested in simple, shallow water environments with and without mismatch in the specification of acoustic parameters (e.g., bathymetry and sound speed).

The results suggest that the use of the additional information from multiple elements does improve both the accuracy and robustness of the localizations. All of the algorithms produced similar results, although the IFACM and the KzFACM algorithms appeared to perform slightly better than the ZFACM algorithm in the presence of mismatch. However, the relative performance of the algorithms appeared to be sensitive to the environment and placement of the source and receivers in the waveguide.

TABLE OF CONTENTS

ACKNOWLEDGEMENTS

I wish to give recognition to:

My wife, Barbara, for her love, patience and support throughout my study at the Naval Postgraduate School. Thanks to her outstanding skills as a mother and a wife, our stay in Monterey will always be remembered with only happy thoughts. Bar, I will always love you, perhaps some days more than others.

My son, Thijs, for his never-ending 'big boy' support, and my two daughters, Sophie and Lotte. Although all three are probably too young to realize, my son being three years old and both girls born in Monterey, they constantly kept my daily life in the correct perspective.

My thesis advisor, Professor Kevin Smith, for his time and support in the past six months. His expertise advice, directions and great help were an enormous support to me in achieving this thesis.

My second reader, Mitchell Shipley, for his time and help. Explaining the theory and especially discussing the results with him was a great help to me

Peer Tas

I. INTRODUCTION

Today, matched field processing (MFP) is one of the most commonly used and successful research techniques for determining the lacking range and depth information for passive sonar systems. In MFP, a comparison is made between some features of a received signal (e.g., amplitude and phase) and those of replica signals generated by a numerical model predicting the field due to a source positioned at each point in the search grid. A match is obtained when the correlation of the two signals, synthetic and true, is at a maximum.

Since 1993, the passive transient localization (PTL) project at the Naval Postgraduate School (NPS) has been studying various algorithms for localizing transient sources based on methods related to MFP. The interest in transient signals is based on the fact that these signals can represent several (some very important) instances of a ship's routine, such as opening of hatches, starting of pumps, popping of the hull, etc.

The primary acoustic signal feature on which most of the NPS effort has focussed has been the signal autocorrelation. The motivation for this was based partly on the lack of absolute travel time information as well as the ability of the autocorrelation to minimize the influence of noise at non-zero lag values. Originally, time-domain autocorrelation matching techniques were analyzed (Miller, et al, 1996, de Kooter, 1997). Subsequent analysis was also performed on frequency-domain autocorrelation matching.

One of the latest studies for the project included the development of MFP algorithms for a single hydrophone receiver and a broadband, transient-like point source (Brune, 1998). The performance of these algorithms was examined numerically in environmental mismatch situations. One of the results of this study was that the frequency-domain autocorrelation matching (FACM) algorithm was most robust for environmental mismatch and in the presence of noise. This was most likely due to less sensitivity to phase mismatch at higher frequencies.

Another recent study for the PTL project examined the success of the FACM algorithm on measured transient data in a shallow water environment (Correa, 1998). In this experiment, a multiple element vertical line array was used. However, only single element analysis was carried out. In that thesis, one of the recommendations for future work was an adaptation of the FACM localization algorithm to include multiple element information. That was the motivation for the present study.

The objective of this thesis is to localize (in range and depth) a broadband, transient-like point source with a vertical line array of 16 hydrophone receivers. Using the geometry of the vertical line array, and re-coding the previously developed FACM algorithm, a number of new MFP algorithms have been developed. These algorithms are a depth- and frequency-domain autocorrelation matching (ZFACM) algorithm, a wavenumber- and frequency-domain autocorrelation matching (KzFACM) algorithm, and an incoherent summation of FACM results of the 16 receiver hydrophones in the array. The robustness of the new algorithms has been tested numerically in different environments and with different environmental mismatches.

The remainder of this thesis consists of four chapters. In Chapter II, the localization algorithms are described. In Chapter III, the propagation model that was used and the necessary data manipulations are discussed. Chapter IV describes the setup of the numerical experiments and the results. Finally, Chapter V provides conclusions and recommendations for future work.

II. LOCALIZATION ALGORITHMS

As mentioned in the Introduction, the realization of the algorithms for this thesis is an adaptation of previous work. Earlier developed algorithms, based on MFP principles, dealt with a single hydrophone receiver and a transient-like, broadband point source. The matching took place between the received signal and a replica. A replica is basically a prediction of the field due to a source positioned at each point in the search grid. A numerical model that will be discussed later generated these predictions. From this previous work, the frequency-domain autocorrelation (FACM) algorithm was concluded to give the best results. Best results were defined as most robust for environmental mismatch, which was most likely due to less sensitivity to phase mismatch at higher frequencies. Therefore, the FACM algorithm is best suited for larger bandwidths and higher frequencies.

The new algorithms are a continuation of this approach, taking the depth information of the multiple hydrophone receivers into account. The transient-like point source is assumed to be omnidirectional. In order to reduce the amount of work to a manageable size, the reciprocity principle was used. This principle states that in an environment without any time variations (e.g., currents), and with identical densities at location A and location B, the acoustic pressure at B from an omnidirectional source at A is identical to the acoustic pressure at A from an equivalent source at B. Therefore, the replicas can be generated from predictions of the acoustic propagation from the hydrophone receiver location to all possible source locations in the search grid.

A. FREQUENCY-DOMAIN AUTOCORRELATION MATCHING

Since autocorrelation matching was initially developed for use in the time-domain, it is more convenient to start the explanation in this domain and convert the results to the frequency-domain. Suppose we have a complex time series P(t) representing a detected transient arrival. The signal autocorrelation in the time-domain can be expressed as

$$T_{PP}(\tau) = \int_{-\infty}^{\infty} P^*(t)P(t+\tau)dt \tag{2-1}$$

or, in terms of the frequency-domain response, as

$$T_{PP}(\tau) = \int_{-\infty}^{\infty} \tilde{P}^*(f)\tilde{P}(f)e^{-i2\pi f\tau}df\,, \tag{2-2}$$

where

$$\tilde{P}(f) = \int_{-\infty}^{\infty} P(t)e^{i2\pi ft}dt\,. \tag{2-3}$$

The normalized autocorrelation function is defined as

$$C_{PP}(\tau) = \frac{T_{PP}(\tau)}{\int_{-\infty}^{\infty}\left|\tilde{P}(f)\right|^2 df}\,. \tag{2-4}$$

For the predicted replica signal R(t), a similar derivation leads to

$$C_{RR}(\tau) = \frac{T_{RR}(\tau)}{\int_{-\infty}^{\infty}\left|\tilde{R}(f)\right|^2 df}\,. \tag{2-5}$$

The time-domain autocorrelation matching (TACM) algorithm is based upon the inner product of the two quantities in Eqs. (2-4) and (2-5). Normalizing this result, it can be expressed (in the time-domain) as

$$A_{TACM} = \frac{\int_{-\infty}^{\infty} C_{RR}^{*}(\tau) C_{PP}(\tau) d\tau}{\left[\int_{-\infty}^{\infty} |C_{RR}(\tau)|^2 d\tau \int_{-\infty}^{\infty} |C_{PP}(\tau)|^2 d\tau\right]^{1/2}} . \qquad (2\text{-}6)$$

Note that this technique attempts to match the relative correlations of separate multipaths in the time-domain signal. These relative correlations occur at lag values corresponding to their temporal separation at the receiver. The temporal separations changed with the sources range and depth position in the environment and provided the information necessary to uniquely localize the source. Previous analyses with algorithms based on this method were found to be highly sensitive to mismatch at high frequencies. Specifically, if the relative arrival times of different multipaths are off by only a few milliseconds, the phase mismatch will be quite large at frequencies of interest for transients (~ 1 kHz).

In the frequency-domain, however, such frequency-dependent effects do not occur where only relative frequencies are relevant. Thus, a frequency-domain autocorrelation matching algorithm was developed. By analogy, the autocorrelation matching in the frequency-domain becomes

$$A_{FACM} = \frac{\int_{-\infty}^{\infty} \tilde{C}_{\tilde{R}\tilde{R}}^{*}(\phi) \tilde{C}_{\tilde{P}\tilde{P}}(\phi) d\phi}{\left[\int_{-\infty}^{\infty} |\tilde{C}_{\tilde{R}\tilde{R}}(\phi)|^2 d\phi \int_{-\infty}^{\infty} |\tilde{C}_{\tilde{P}\tilde{P}}(\phi)|^2 d\phi\right]^{1/2}} , \qquad (2\text{-}7)$$

where $\tilde{C}_{\tilde{P}\tilde{P}}$ and $\tilde{C}_{\tilde{R}\tilde{R}}$ are the frequency-domain autocorrelations of the transient signal and of the replica, respectively. Since

$$\int_{-\infty}^{\infty} \tilde{C}^{*}_{\tilde{R}\tilde{R}}(\phi)\tilde{C}_{\tilde{P}\tilde{P}}(\phi)d\phi = \frac{\int_{-\infty}^{\infty} d\phi \left[\int_{-\infty}^{\infty} dt |R(t)|^2 e^{-i2\pi\phi t}\right]\left[\int_{-\infty}^{\infty} dt' |P(t')|^2 e^{i2\pi\phi t'}\right]}{\int_{-\infty}^{\infty} |R(t)|^2 dt \int_{-\infty}^{\infty} |P(t)|^2 dt}$$

$$= \frac{\int_{-\infty}^{\infty} dt |R(t)|^2 \int_{-\infty}^{\infty} dt' |P(t')|^2 \left[\int_{-\infty}^{\infty} d\phi e^{i2\pi\phi(t'-t)}\right]}{\int_{-\infty}^{\infty} |R(t)|^2 dt \int_{-\infty}^{\infty} |P(t)|^2 dt}$$

$$= \frac{\int_{-\infty}^{\infty} |R(t)|^2 |P(t)|^2 dt}{\int_{-\infty}^{\infty} |R(t)|^2 dt \int_{-\infty}^{\infty} |P(t)|^2 dt} , \qquad (2\text{-}8)$$

Eq. (2-7) can be rewritten as

$$A_{FACM} = \frac{\int_{-\infty}^{\infty} |R(t)|^2 |P(t)|^2 dt}{\left[\int_{-\infty}^{\infty} |R(t)|^4 dt \int_{-\infty}^{\infty} |P(t)|^4 dt\right]^{1/2}} . \qquad (2\text{-}9)$$

To reduce the influence of noise and to emphasize the comparison between the cross terms, it is necessary to remove the zero-lag of the autocorrelation function. This is equivalent to removing the mean squared amplitude of the signal in the time-domain. Therefore, defining

$$|R'(t)|^2 = |R(t)|^2 - \left\langle |R(t)|^2 \right\rangle \tag{2-10}$$

and

$$|P'(t)|^2 = |P(t)|^2 - \left\langle |P(t)|^2 \right\rangle , \tag{2-11}$$

where in both cases the average is over all times, Eq. (2-9) becomes

$$A_{FACM} = \frac{\int_{-\infty}^{\infty} |R'(t)|^2 |P'(t)|^2 dt}{\left[\int_{-\infty}^{\infty} |R'(t)|^4 dt \int_{-\infty}^{\infty} |P'(t)|^4 dt \right]^{1/2}} . \tag{2-12}$$

In order to find the optimal match, a search parameter τ will be introduced which allows us to slide the replica signal in time. This procedure is necessary since absolute time information is not available. The FACM algorithm is then based on evaluation of the function

$$A_{FACM} = \max_{\tau} \left\{ \frac{\int_{-\infty}^{\infty} |R'(t+\tau)|^2 |P'(t)|^2 dt}{\left[\int_{-\infty}^{\infty} |R'(t)|^4 dt \int_{-\infty}^{\infty} |P'(t)|^4 dt \right]^{1/2}} \right\} , \tag{2-13}$$

where $\max_{\tau}$ is the maximum value of the function for any value of the search parameter.

In previous thesis work, a MATLAB® implementation of the algorithm based on Eq. (2-13) was used to generate the ambiguity surfaces for a single hydrophone receiver. The sliding- τ operation was performed by a multiplication in the frequency-domain and an inverse FFT operation, as will be shown by the following derivation. Let $g(t) \equiv |P'(t)|^2$ and $h(t) \equiv |R'(t)|^2$, then

$$g(t) = \int_{-\infty}^{\infty} e^{-i2\pi ft} G(f) df \quad , \tag{2-14}$$

and

$$h(t) = \int_{-\infty}^{\infty} e^{-i2\pi ft} H(f) df \quad , \tag{2-15}$$

$$h(t+\tau) = \int_{-\infty}^{\infty} e^{-i2\pi(t+\tau)t} H(f) df = \int_{-\infty}^{\infty} e^{-i2\pi ft} H(f) e^{-i2\pi f\tau} df \quad .$$

The numerator of Eq. (2-13) becomes

$$I(\tau) = \int_{-\infty}^{\infty} h(t+\tau) g(t) dt \quad . \tag{2-16}$$

Since $h(t)$ is a real function, then $h(t) = h^*(t)$ and

$$I(\tau) = \int_{-\infty}^{\infty} h^*(t+\tau) g(t) dt$$

$$= \int_{-\infty}^{\infty} \left[\int_{-\infty}^{\infty} e^{i2\pi ft} H^*(f) e^{i2\pi f\tau} df \right] \left[\int_{-\infty}^{\infty} e^{-i2\pi f' t} G(f') df' \right] dt$$

$$= \int_{-\infty}^{\infty} \int_{-\infty}^{\infty} \left[H^*(f) G(f') e^{i2\pi f\tau} \int_{-\infty}^{\infty} e^{-i2\pi(f'-f)t} dt \right] df' df$$

$$= \int_{-\infty}^{\infty} H^*(f)G(f)e^{i2\pi f\tau}df \ . \qquad (2\text{-}17)$$

Thus, after computing $|P'(t)|^2$ and $|R'(t)|^2$ and the corresponding frequency-domain representations $G(f)$ and $H(f)$, the function $I(\tau)$ can easily be computed. The maximum value of $I(\tau)$ then corresponds to the maximum of the numerator in Eq. (2-13).

B. INCOHERENT SUMMATION

The vertical line array has 16 omni-directional hydrophone receivers. The most straightforward extension of the FACM algorithm is the incoherent summation of the FACM results of each of the single hydrophone receivers of the array. As mentioned earlier, the FACM results are displayed as ambiguity surfaces. Therefore, the incoherent summation (IFACM) algorithm can best be seen as the averaged overlay result of 16 ambiguity surfaces of single hydrophone receivers. This can be defined simply as

$$A_{IFACM} = \frac{1}{16}\sum_{i=1}^{16}\left[\max_{\tau}\left\{\frac{\int_{-\infty}^{\infty}|R'(z_i,t+\tau)|^2|P'(z_i,t)|^2dt}{\left[\int_{-\infty}^{\infty}|R'(z_i,t)|^4dt\int_{-\infty}^{\infty}|P'(z_i,t)|^4dt\right]^{1/2}}\right\}\right] . \qquad (2\text{-}18)$$

C. DEPTH- AND FREQUENCY-DOMAIN AUTOCORRELATION MATCHING

A more advanced extension of the FACM algorithm is the depth- and frequency-domain autocorrelation matching (ZFACM) algorithm, where the hydrophone receiver depths are incorporated into the autocorrelation calculations as a second 'dimension'. This can also be thought of as joint autocorrelation matching.

The following derivation of the ZFACM algorithm has the same flow as the 'one-dimensional' FACM. This time, the derivation will start directly in the depth- and frequency-domain. A necessary additional remark beforehand concerns Fourier-pairs. The depth- and vertical wavenumber-values, k_z, form a Fourier-pair, similar to the probably better known Fourier-pair, frequency- and time-values. Thus, we will simplify our development by taking advantage of such symmetries.

Because all the hydrophone receivers are located at a specific depth, the transient arrival, as detected by the whole vertical line array, can be expressed by a complex time- and depth-series $P(t,z)$. With a Fourier transform on the time-domain component of this series, it will become a complex depth- and frequency-series $P(z,f)$.

The signal autocorrelation in the depth- and frequency-domain may be written

$$F_{PP}(\xi,\phi) = \int_{-\infty}^{\infty}\int_{-\infty}^{\infty} P^*(z,f)P(z+\xi,f+\phi)dzdf \quad . \tag{2-19}$$

Defining

$$P(z,f)=\frac{1}{2\pi}\int_{-\infty}^{\infty}\int_{-\infty}^{\infty}P(k_z,t)e^{ik_z z}e^{i2\pi ft}dk_z dt \qquad (2\text{-}20)$$

$$P(z,f)=\boldsymbol{F}^{-2}\left[P(k_z,t)\right]$$

and

$$P(k_z,t)=\int_{-\infty}^{\infty}\int_{-\infty}^{\infty}P(z,f)e^{-ik_z z}e^{-i2\pi ft}dzdf \qquad (2\text{-}21)$$

$$P(k_z,t)=\boldsymbol{F}^{2}\left[P(z,f)\right]\ ,$$

where $\boldsymbol{F}^{2}$ and $\boldsymbol{F}^{-2}$ indicate the two-dimensional forward and inverse Fourier transforms, respectively, Eq. (2-19) can be rewitten as

$$F_{PP}(\xi,\phi)=$$

$$\int_{-\infty}^{\infty}\int_{-\infty}^{\infty}\left[\frac{1}{2\pi}\int_{-\infty}^{\infty}\int_{-\infty}^{\infty}P^{*}(k_z,t)e^{-ik_z z}e^{-i2\pi ft}dk_z dt\right]\left[\frac{1}{2\pi}\int_{-\infty}^{\infty}\int_{-\infty}^{\infty}P(k_z',t')e^{ik_z'(z+\xi)}e^{i2\pi'(f+\phi)}dk_z' dt'\right]dzdf$$

$$=\frac{1}{2\pi}\int_{-\infty}^{\infty}\int_{-\infty}^{\infty}\int_{-\infty}^{\infty}\int_{-\infty}^{\infty}dtdt'dk_z dk_z' P^{*}(k_z,t)P(k_z',t')e^{i2\pi\phi t'}e^{i\xi k_z'}\left[\frac{1}{2\pi}\int_{-\infty}^{\infty}\int_{-\infty}^{\infty}e^{i2\pi f(t'-t)}e^{iz(k_z'-k_z)}dzdf\right]$$

$$=\frac{1}{2\pi}\int_{-\infty}^{\infty}\int_{-\infty}^{\infty}P^{*}(k_z,t)P(k_z,t)e^{i2\pi\phi t}e^{i\xi k_z}dtdk_z$$

$$=\boldsymbol{F}^{-2}\left[\left|P(k_z,t)\right|^{2}\right]\ . \qquad (2\text{-}22)$$

The normalized joint autocorrelation becomes

$$C_{PP}(\xi,\phi)=\frac{\boldsymbol{F}^{-2}\left[\left|P(k_z,t)\right|^2\right]}{\frac{1}{2\pi}\int_{-\infty}^{\infty}\int_{-\infty}^{\infty}\left|P(k_z,t)\right|^2 dk_z dt} \quad . \tag{2-23}$$

For the predicted replica signal $R(z,f)$, a similar derivation leads to

$$C_{RR}(\xi,\phi)=\frac{\boldsymbol{F}^{-2}\left[\left|R(k_z,t)\right|^2\right]}{\frac{1}{2\pi}\int_{-\infty}^{\infty}\int_{-\infty}^{\infty}\left|R(k_z,t)\right|^2 dk_z dt} \quad . \tag{2-24}$$

Since we want to emphasize the matching of the non-zero lag values, reducing the influence of noise, these zero-lag values should be removed. This can be accomplished by removing the means from the wavenumber- and time-domain, i.e.

$$C'_{PP}(\xi,\phi)=\frac{\boldsymbol{F}^{-2}\left[\left|P'(k_z,t)\right|^2\right]}{\frac{1}{2\pi}\int_{-\infty}^{\infty}\int_{-\infty}^{\infty}\left|P'(k_z,t)\right|^2 dk_z dt} \tag{2-25}$$

and

$$C'_{RR}(\xi,\phi)=\frac{\boldsymbol{F}^{-2}\left[\left|R'(k_z,t)\right|^2\right]}{\frac{1}{2\pi}\int_{-\infty}^{\infty}\int_{-\infty}^{\infty}\left|R'(k_z,t)\right|^2 dk_z dt} \quad , \tag{2-26}$$

where

$$\left|P'(k_z,t)\right|^2 = \left|P(k_z,t)\right|^2 - \left\langle \left|P(k_z,t)\right|^2 \right\rangle \tag{2-27}$$

and

$$\left|R'(k_z,t)\right|^2 = \left|R(k_z,t)\right|^2 - \left\langle \left|R(k_z,t)\right|^2 \right\rangle \ . \tag{2-28}$$

In both cases the averages are taken over time and wavenumber. The ambiguity surface is then based on

$$A_{ZFACM} = \frac{\int_{-\infty}^{\infty}\int_{-\infty}^{\infty} C'^{*}_{RR}(\xi,\phi)C'_{PP}(\xi,\phi)d\xi d\phi}{\left[\int_{-\infty}^{\infty}\int_{-\infty}^{\infty}\left|C'_{RR}(\xi,\phi)\right|^2 d\xi d\phi \int_{-\infty}^{\infty}\int_{-\infty}^{\infty}\left|C'_{PP}(\xi,\phi)\right|^2 d\xi d\phi\right]^{1/2}} \ , \tag{2-29}$$

where

$$\int_{-\infty}^{\infty}\int_{-\infty}^{\infty} C'^{*}_{RR}(\xi,\phi)C'_{PP}(\xi,\phi)d\xi d\phi =$$

$$\frac{\int_{-\infty}^{\infty}\int_{-\infty}^{\infty} d\xi d\phi \left[\frac{1}{2\pi}\int_{-\infty}^{\infty}\int_{-\infty}^{\infty}\left|R'(k_z,t)\right|^2 e^{-i\xi k_z} e^{-i2\pi\phi t} dk_z dt\right]\left[\frac{1}{2\pi}\int_{-\infty}^{\infty}\int_{-\infty}^{\infty}\left|P'(k'_z,t')\right|^2 e^{i\xi k'_z} e^{i2\pi\phi t'} dk'_z dt'\right]}{\frac{1}{(2\pi)^2}\int_{-\infty}^{\infty}\int_{-\infty}^{\infty}\left|R'(k_z,t)\right|^2 dk_z dt \cdot \int_{-\infty}^{\infty}\int_{-\infty}^{\infty}\left|P'(k\ ,t)\right|^2 dk_z dt}$$

$$= \frac{\frac{1}{2\pi}\int_{-\infty}^{\infty}\int_{-\infty}^{\infty} dk_z dt \int_{-\infty}^{\infty}\int_{-\infty}^{\infty} dk'_z dt' \left|R'(k_z,t)\right|^2 \left|P'(k'_z,t')\right|^2 \cdot \left[\frac{1}{2\pi}\int_{-\infty}^{\infty}\int_{-\infty}^{\infty} d\xi d\phi e^{i\xi(k'_z-k_z)} e^{i2\pi\phi(t'-t)}\right]}{\frac{1}{(2\pi)^2}\int_{-\infty}^{\infty}\int_{-\infty}^{\infty}\left|R'(k_z,t)\right|^2 dk_z dt \cdot \int_{-\infty}^{\infty}\int_{-\infty}^{\infty}\left|P'(k\ ,t)\right|^2 dk_z dt}$$

$$= \frac{\frac{1}{2\pi}\int_{-\infty-\infty}^{\infty}\int^{\infty}\left|R'(k_z,t)\right|^2\left|P'(k_z,t)\right|^2 dk_z dt}{\frac{1}{(2\pi)^2}\int_{-\infty-\infty}^{\infty}\int^{\infty}\left|R'(k_z,t)\right|^2 dk_z dt \cdot \int_{-\infty-\infty}^{\infty}\int^{\infty}\left|P'(k\ ,t)\right|^2 dk_z dt} \quad . \tag{2-30}$$

Then, also

$$\int_{-\infty-\infty}^{\infty}\int^{\infty}\left|C'_{RR}(\xi,\phi)\right|^2 d\xi d\phi = \frac{\frac{1}{2\pi}\int_{-\infty-\infty}^{\infty}\int^{\infty}\left|R'(k_z,t)\right|^4 dk_z dt}{\left[\frac{1}{2\pi}\int_{-\infty-\infty}^{\infty}\int^{\infty}\left|R'(k_z,t)\right|^2 dk_z dt\right]^2} \tag{2-31}$$

and

$$\int_{-\infty-\infty}^{\infty}\int^{\infty}\left|C'_{PP}(\xi,\phi)\right|^2 d\xi d\phi = \frac{\frac{1}{2\pi}\int_{-\infty-\infty}^{\infty}\int^{\infty}\left|P'(k_z,t)\right|^4 dk_z dt}{\left[\frac{1}{2\pi}\int_{-\infty-\infty}^{\infty}\int^{\infty}\left|P'(k_z,t)\right|^2 dk_z dt\right]^2} \quad . \tag{2-32}$$

Finally, the ZFACM function can be expressed as

A_{ZFACM} =

$$\frac{\left[\frac{1}{2\pi}\int_{-\infty-\infty}^{\infty}\int^{\infty}\left|R'(k_z,t)\right|^2\left|P'(k_z,t)\right|^2 dk_z dt\right]}{\left[\frac{1}{2\pi}\int_{-\infty-\infty}^{\infty}\int^{\infty}\left|R'(k_z,t)\right|^2 dk_z dt\right]\left[\frac{1}{2\pi}\int_{-\infty-\infty}^{\infty}\int^{\infty}\left|P'(k_z,t)\right|^2 dk_z dt\right]} \cdot$$

$$\frac{\left[\frac{1}{2\pi}\int_{-\infty-\infty}^{\infty}\int^{\infty}\left|R'(k_z,t)\right|^2 dk_z dt\right]\left[\frac{1}{2\pi}\int_{-\infty-\infty}^{\infty}\int^{\infty}\left|P'(k_z,t)\right|^2 dk_z dt\right]}{\left[\frac{1}{(2\pi)^2}\int_{-\infty-\infty}^{\infty}\int^{\infty}\left|R'(k_z,t)\right|^4 dk_z dt \cdot \int_{-\infty-\infty}^{\infty}\int^{\infty}\left|P'(k_z,t)\right|^4 dk_z dt\right]^{1/2}}$$

$$= \frac{\int_{-\infty}^{\infty}\int_{-\infty}^{\infty} \left|R'(k_z,t)\right|^2 \left|P'(k_z,t)\right|^2 dk_z dt}{\left[\int_{-\infty}^{\infty}\int_{-\infty}^{\infty} \left|R'(k_z,t)\right|^4 dk_z dt \cdot \int_{-\infty}^{\infty}\int_{-\infty}^{\infty} \left|P'(k_z,t)\right|^4 dk_z dt\right]^{1/2}} . \qquad (2\text{-}33)$$

Like with the FACM derivation, since absolute time information is not available, a search parameter τ will be introduced in order to find the optimal match in time. Also, a search parameter K will be introduced as the wavenumber-domain equivalent. Since the absolute depths of the receivers (hence absolute wavenumber) are exactly known, the second search parameter seems to be obsolete. However, the autocorrelation matching has become a 'two-dimensional' matching, therefore both search parameters are introduced. These search parameters allow us to slide the replica signal in wavenumber and time. The ZFACM function then becomes

$$A_{ZFACM} = \max_{\mathrm{K},\tau} \left\{ \frac{\int_{-\infty}^{\infty}\int_{-\infty}^{\infty} \left|R'(k_z+\mathrm{K},t+\tau)\right|^2 \left|P'(k_z,t)\right|^2 dk_z dt}{\left[\int_{-\infty}^{\infty}\int_{-\infty}^{\infty} \left|R'(k_z,t)\right|^4 dk_z dt \cdot \int_{-\infty}^{\infty}\int_{-\infty}^{\infty} \left|P'(k_z,t)\right|^4 dk_z dt\right]^{1/2}} \right\} . \qquad (2\text{-}34)$$

The sliding operation is again performed in the alternate domain in a manner similar to that described in the previous description of the FACM algorithm.

D. WAVENUMBER- AND FREQUENCY-DOMAIN AUTOCORRELATION MATCHING

Another advanced extension of the FACM algorithm is the wavenumber- and frequency-domain autocorrelation matching (KzFACM) algorithm. This time, the vertical wavenumber-values k_z are incorporated into the autocorrelation calculations as the second 'dimension'.

The derivation of the KzFACM algorithm has exactly the same flow as the ZFACM derivation, and therefore the larger part of it will be left out. A complex time- and depth-series $P(t,z)$, as detected by the whole vertical line array, can express the transient arrival. With a Fourier transform on both domain components of this series, it will become a complex wavenumber- and frequency-series $P(k_z,f)$.

A similar derivation as for the ZFACM function leads to the final result for the KzFACM function,

$$A_{KzFACM} = \max_{\xi,\tau}\left\{\frac{\int_{-\infty}^{\infty}\int_{-\infty}^{\infty}\left|R'(z+\xi,t+\tau)\right|^2\left|P'(z,t)\right|^2 dzdt}{\left[\int_{-\infty}^{\infty}\int_{-\infty}^{\infty}\left|R'(z,t)\right|^4 dzdt\cdot\int_{-\infty}^{\infty}\int_{-\infty}^{\infty}\left|P'(z,t)\right|^4 dzdt\right]^{1/2}}\right\}, \qquad (2\text{-}35)$$

where ξ and τ are the search parameters for the depth- and time-domain, respectively. Again, since the autocorrelation matching has become a 'two-dimensional' matching, both search parameters are introduced. These search parameters allow us to slide the replica signal in depth and time.

It is important to note the physical interpretation of these autocorrelation matching algorithms. As has been shown, the autocorrelation matching in one domain may be computed from the square amplitude in the Fourier domain. Thus, for example, the FACM algorithm is actually performing a squared amplitude (envelope) matching in the time-domain. In the context of such envelope matching, it is perhaps more obvious that this algorithm will be less sensitive to time-domain phase mismatch. Therefore, an examination of the previous work suggests that the time-domain envelopes provide a more stable acoustic signature for transient localization than the corresponding frequency-domain envelopes.

The relationship between domains should be kept in mind when evaluating the following results presented in this thesis. Specifically, the depth- and frequency-domain autocorrelation matching is equivalent to a squared amplitude matching in the wavenumber- and time-domain. Furthermore, it is worthwhile noting that the results in the wavenumber-domain may also be associated with similar algorithms employed in beam-space.

THIS PAGE INTENTIONALLY LEFT BLANK

III. NUMERICAL METHOD

A. MONTEREY-MIAMI PARABOLIC EQUATION (MMPE) PROPAGATION MODEL

In this chapter, the propagation model used to predict the arrival structure replicas at a receiver location due to a point source at a test location will be described. Also, the methods for processing the outputs of the model to produce the time-domain arrival structure predictions will be explained.

In order to generate the replicas that simulated the received signals from a synthetic source on defined points of a two dimensional search space (depth versus range), the Monterey-Miami Parabolic Equation (MMPE) propagation model (Smith, 1999) was used. In this chapter, the general theory behind the parabolic equation model will be introduced, as well as the method used for its implementation – the split-step Fourier method (Hardin and Tappert, 1973).

The inhomogeneous wave equation for the acoustic pressure $p(\vec{x},t)$ in a medium with sound speed $c(\vec{x})$ and density $\rho(\vec{x})$ can be expressed as (Jensen, et al, 1994)

$$\rho(\vec{x})\nabla\cdot\left(\frac{\nabla p(\vec{x},t)}{\rho(\vec{x})}\right)-\frac{1}{c(\vec{x})^2}\frac{\partial^2 p(\vec{x},t)}{\partial t^2}=S(\vec{x},t)\ . \qquad (3\text{-}1)$$

The parabolic equation model is based on an approximation of the Helmholtz wave equation in a cylindrical coordinate system. Because of the ocean's relative shallowness compared to horizontal propagation distance for the majority of the environments, it is well suited for a description in cylindrical coordinates. Assuming a time harmonic solution, the Helmholtz equation takes the form

$$\frac{1}{r}\frac{\partial}{\partial r}\left(r\frac{\partial p(r,z,\phi,f)}{\partial r}\right)+\frac{1}{r^2}\frac{\partial^2 p(r,z,\phi,f)}{\partial \phi^2}+\frac{\partial^2 p(r,z,\phi,f)}{\partial z^2}$$
$$+k_0^2 n^2(r,z,\phi)p(r,z,\phi,f)=-4\pi P_0\delta(\vec{r}-\vec{r}_s)\ , \qquad (3\text{-}2)$$

where

$$P(r,z,\phi,t)=p(r,z,\phi,f)e^{-i2\pi ft}\ . \qquad (3\text{-}3)$$

The reference wavenumber is related to a reference sound speed, c_0, by

$$k_0=\frac{\omega}{c_0}\ , \qquad (3\text{-}4)$$

and the acoustic index of refraction is defined by

$$n=\frac{c_0}{c(r,z,\phi)}\ . \qquad (3\text{-}5)$$

Note that in this derivation the density variations are neglected. By defining the effective index of refraction which contains the appropriate additional terms, the influence of the density differences at the water-bottom interface can be included (e.g., Tappert, 1977).

By assuming that the ocean acts as a waveguide with a cylindrical coordinate system, acoustic energy is mainly propagated outward from a source in the horizontal direction. Therefore, the pressure field can be approximated by

$$p(r,z,\phi,f)=\Psi(r,z,\phi,f)H_0^{(1)}(k_0 r)\ , \qquad (3\text{-}6)$$

where $\Psi_f(r,z,\phi,f)$ is a slowly varying envelope modulating the outgoing zero-th order Hankel function of the first kind $H_0^{(1)}(k_0 r)$. Taking advantage of the far-field $(k_0 r >> 1)$ asymptotic approximation of the Hankel function, Eq. (3-6) can be rewritten as

$$p(r,z,\phi,f) = \frac{P_0 R_0}{\sqrt{r}} \Psi(r,z,\phi,f) e^{ik_0 r} \ , \tag{3-7}$$

normalized such that at the reference range $r = R_0$, $|p| = P_0$. Substituting Eq. (3-7) into Eq. (3-2) and dropping the source term on the right hand side gives

$$\frac{\partial^2 \Psi}{\partial r^2} + i2k_0 \frac{\partial \Psi}{\partial r} + \frac{1}{r^2}\frac{\partial^2 \Psi}{\partial \phi^2} + \frac{\partial^2 \Psi}{\partial z^2} + \left[k_0^2 (n^2 - 1) + \frac{1}{4r^2} \right] \Psi = 0 \ . \tag{3-8}$$

Neglecting the azimuthal coupling and the far-field terms, and dropping the first term due to the slow modulations of the envelope function, Eq. (3-8) can be rewritten as

$$\frac{i}{k_0}\frac{\partial \Psi}{\partial r} = -\frac{1}{2k_0}\frac{\partial^2 \Psi}{\partial z^2} - \frac{1}{2}(n^2 - 1)\Psi \ . \tag{3-9}$$

Defining the operators

$$T_{op} = -\frac{1}{2k_0}\left(\frac{\partial^2}{\partial z^2}\right) \ , \tag{3-10}$$

and

$$U_{op} = -\frac{1}{2}(n^2 - 1) \ , \tag{3-11}$$

Eq. (3-9) can be written as

$$\frac{i}{k_0}\frac{\partial \Psi}{\partial r} = \left(T_{op} + U_{op}\right)\Psi \ . \tag{3-12}$$

Equation (3-12) is known as the "standard" parabolic equation (SPE) (Tappert, 1977), with accurate solutions limited to a half beam width of 10° to 20° for the propagation angle. For this work, in order to extend this limit to 40° to 70°, a higher order wide-angle parabolic equation (WAPE) approximation (Thomson and Chapman, 1983) is used. Its operators are defined by

$$T_{WAPE} = 1 - \sqrt{1 + \frac{1}{k_0^2}\frac{\partial^2}{\partial z^2}} \ , \tag{3-13}$$

and

$$U_{WAPE} = -(n-1) \ . \tag{3-14}$$

The MMPE uses the split-step Fourier (SSF) method in order to solve the parabolic equation numerically. This algorithm integrates the solution in range by applying the T_{WAPE} and the U_{WAPE} operators in the k_z - domain and the z - domain, respectively, where each operator is simply a scalar multiplier. In the k_z - space the wide angle $\hat{T}_{WAPE}$ operator is defined as

$$\hat{T}_{WAPE}(k_z) = 1 - \sqrt{\left(1 - \frac{k_z^2}{k_0^2}\right)} \ . \tag{3-15}$$

The algorithm for stepping in range from r to $r+\Delta r$ is the $O(\Delta r^3)$ accurate centered-step scheme (Jensen, et al., 1994), which can now be expressed as

$$\Psi(r+\Delta r,z)=e^{-ik_0\Delta r U_{WAPE}(r+\Delta r,z)}\boldsymbol{F}^{-1}\left\{e^{-ik_0\Delta r\hat{T}_{WAPE}(k_z)}\boldsymbol{F}\left[e^{-ik_0\frac{\Delta r}{2}U_{WAPE}(r,z)}\Psi(r,z)\right]\right\}, \qquad (3\text{-}16)$$

B. DATA MANIPULATIONS

The output of the MMPE model is in the form of the field function Ψ (both magnitude and phase) and has been referenced to unit magnitude at 1 m. The field function is computed at the defined spatial grid points. The pressure is defined in terms of the field function Ψ by Eq. (3-7).

Broadband results were obtained by running the MMPE model for all discrete frequencies in the chosen bandwidth. The travel time results were realized by performing a Fourier synthesis and a necessary multiplication by some window-function, $S(f)$. The complex arrival structure of the pressure field can then be written as

$$P(r,z,t)=\int_{-\infty}^{\infty}S(f)p(r,z,f)e^{-i2\pi ft}df=\frac{P_0R_0}{\sqrt{r}}\int_{-\infty}^{\infty}S(f)e^{ik_0r}\Psi(r,z,f)e^{-i2\pi ft}df\ . \qquad (3\text{-}17)$$

By defining the reduced time $T=t-\left(\frac{r}{c_0}\right)$, the phase factor $e^{ik_0r}=e^{i2\pi f\frac{r}{c_0}}$ can be neglected, such that

$$P(r,z,T)=\frac{P_0R_0}{\sqrt{r}}\int_{-\infty}^{\infty}S(f)\Psi(r,z,\phi)e^{-i2\pi fT}df\ . \qquad (3\text{-}18)$$

Note that the use of a reduced time does not influence the autocorrelation function.

For all algorithms, the same window function was used. The modeled pulse transmission had a center frequency of 1400 Hz with a bandwidth of 900 Hz. The temporal spread at maximum range was ~ 0.25 seconds. In order to avoid any errors due to aliasing, the minimum width of the time-domain window should be larger than this. Therefore, 512 frequency bins were computed over the bandwidth, which produced a time window of 0.569 seconds. Over this bandwidth, a simple Hanning window was applied.

To remove the mean from the signals, as required by Eqs. (2.10) and (2.11), without introducing a discontinuous removal of the d.c.-component in the Fourier domain, the following approach was taken. To remove the mean from $|P(t)|^2$, for example, the series $|P(t)|^2$ was first transferred to the frequency – domain. A smooth Hanning-taper was then applied to the 16 bins around d.c., followed by a transformation back to the time-domain. The consequence of this filtering process was to remove the mean and filter only the lowest frequency components.

For both the source data and replica data, the field information from the output of the MMPE propagation model was used as input for the autocorrelation matching algorithms. The structure of the MMPE output file is as follows. After a header with general information, the amplitude and phase values of the field function are stored at every depth point for the first range step and frequency bin. This is followed by the same data for the next range step, and continued for all range steps out to the maximum range for the first frequency bin. After reaching the maximum range, the procedure begins again for the next frequency bin. This

process repeats itself until all frequencies have been computed. The result of this ordering, from innermost to outermost loops, is depth – range – frequency.

In order to develop the autocorrelation matching algorithms as time-efficient as possible, the input files should be read in such a way to obtain the full frequency bandwidth at each spatial gridpoint. Therefore, the MMPE output files had to be reordered first. For this reordering procedure an existing FORTRAN® algorithm was used. The result of this reordering process produced data files organized from innermost to outermost as frequency – depth – range.

THIS PAGE INTENTIONALLY LEFT BLANK

IV. EXPERIMENTAL SETUP AND RESULTS

Several numerical experiments were conducted in order to gain insight into the performance of the autocorrelation matching algorithms. For all experiments both the transient and the replica field functions were calculated with the MMPE propagation model. The field function of a replica represents those values received from a test source positioned at each defined point in the search area. The results of the autocorrelation matching algorithms are presented in an ambiguity surface. For the theoretical situation where the field functions of the transient and the replica are 100% the same, the ambiguity surface will show a maximum exactly at the source location of unit amplitude (with proper normalization).

Three environments were selected to test the robustness of the algorithms. The first environment was mainly used to baseline the performance of the algorithms. For this case, the environment was exactly known for both the transient and the replicas. For each of the other two environments, three different situations were tested: the all-known situation, in which the environments for both the transient and replica data were exactly the same; an environmental mismatch in the sound speed profile; and an environmental mismatch in the bottom bathymetry. Mismatch details will be discussed later.

The search area had a total range of 10 km and a depth of 100 m. The resolution of the ambiguity surface is 40 m in range and 1.56 m in depth. In some situations a 'zoomed-in' ambiguity surface was calculated with a window of 500 m in range and 100 m in depth around the source location. This 'zoomed-in' version had a resolution of 3.33 m in range and 0.78 m in depth.

For all experiments the transient had a 1400 Hz center frequency with a 900 Hz bandwidth. This bandwidth was sampled over 512 points, corresponding to a frequency resolution of 1.7578125 Hz and a time window of width 0.569 seconds.

The modeled vertical line array had a total length of 2.93 m. This is approximately the length of a modern operational array. The array consisted of 16 omni-directional hydrophone receivers. This number was chosen in part because the calculation time of the required Fourier transforms can be significantly reduced if the total number of elements (in this case, hydrophones) is a power of two. The element spacing was 0.195 m. This element spacing coincided with the nominal model depth grid spacing, so that all hydrophones in the array could be positioned exactly on a grid point. For each environment the line array was positioned at two different depth-ranges, realizing a shallow aperture spanning 19.43 m to 22.36 m, and a deep aperture spanning 54.79 m to 57.71 m.

As stated earlier, the ambiguity surfaces presented are the numerical result of an autocorrelation matching function. Its maximum value is unity since the autocorrelation matching function is normalized. This maximum value will occur at the actual source location, but only in the theoretical situation that the predicted field function is identical to the source field function. For all the other situations, more areas with high correlation values can be expected on the ambiguity surface. These areas are commonly referred to as 'sidelobes' and would correspond to false targets in an operational system. Also, predicted source positions are not pinpoint locations but finite area peaks of high correlation. These areas give size and shape to the localization 'footprint' (Tolstoy, 1993). The ambiguity surface of an algorithm is described by the number and magnitude of the sidelobes and the area of the footprint.

For the ambiguity surfaces, the axes are defined as followed. Along the x-axis the range in km is displayed. This range can either be the full range search area of 10 km, or the 'zoomed-in' search area of 500 m around the source location. Along the y-axis the depth in m of the search area is displayed. In all cases, the depth ranges from 0 m at the surface to the maximum depth of 100 m. The vertical line array is not shown in the ambiguity surface. The array is always

located at a range of 0 km, and its depth is either the shallow location or the deep location. Next to the ambiguity surface a colorbar is shown. This colorbar has a high limit equal to the maximum value of the autocorrelation matching function, and a defined low limit. In most cases this lower limit is set to 0.6, although in some cases this limit is adjusted to improve the readability of the ambiguity surface.

A. CASE 1: ISOSPEED SOUND SPEED PROFILE

For this case the source was located at a range of 5.2 km from the vertical line array and at a depth of 33 m. The sound speed was range-independent with an isospeed profile of 1500 m/s. The density of water was assumed to be 1.0 g/cm^3. The bottom was chosen to be completely flat at a depth of 100 m. Its compressional sound speed was 1600 m/s, the density 1.5 g/cm^3, and the attenuation 0.1 dB/km/Hz. This simple type of environment is commonly referred to as a Pekeris waveguide.

In the following series of figures, the ambiguity surfaces are shown for the shallow array for the three different algorithms: the incoherent summation (IFACM) algorithm (Fig. 4.1), the wavenumber- and frequency-domain autocorrelation matching (KzFACM) algorithm (Fig. 4.2), and the depth- and frequency-domain autocorrelation matching (ZFACM) algorithm (Fig. 4.3). For all three, both the full range and the 'zoomed-in' surfaces are displayed.

For the IFACM, the full range ambiguity surface is shown over its full dynamic range (Fig. 4.1(a)) and over an adjusted dynamic range (Fig. 4.1(b)). Since adjusting the dynamic range (without changing any of the autocorrelation matching results) will improve the readability, all other ambiguity surfaces are only presented with adjusted dynamic ranges.

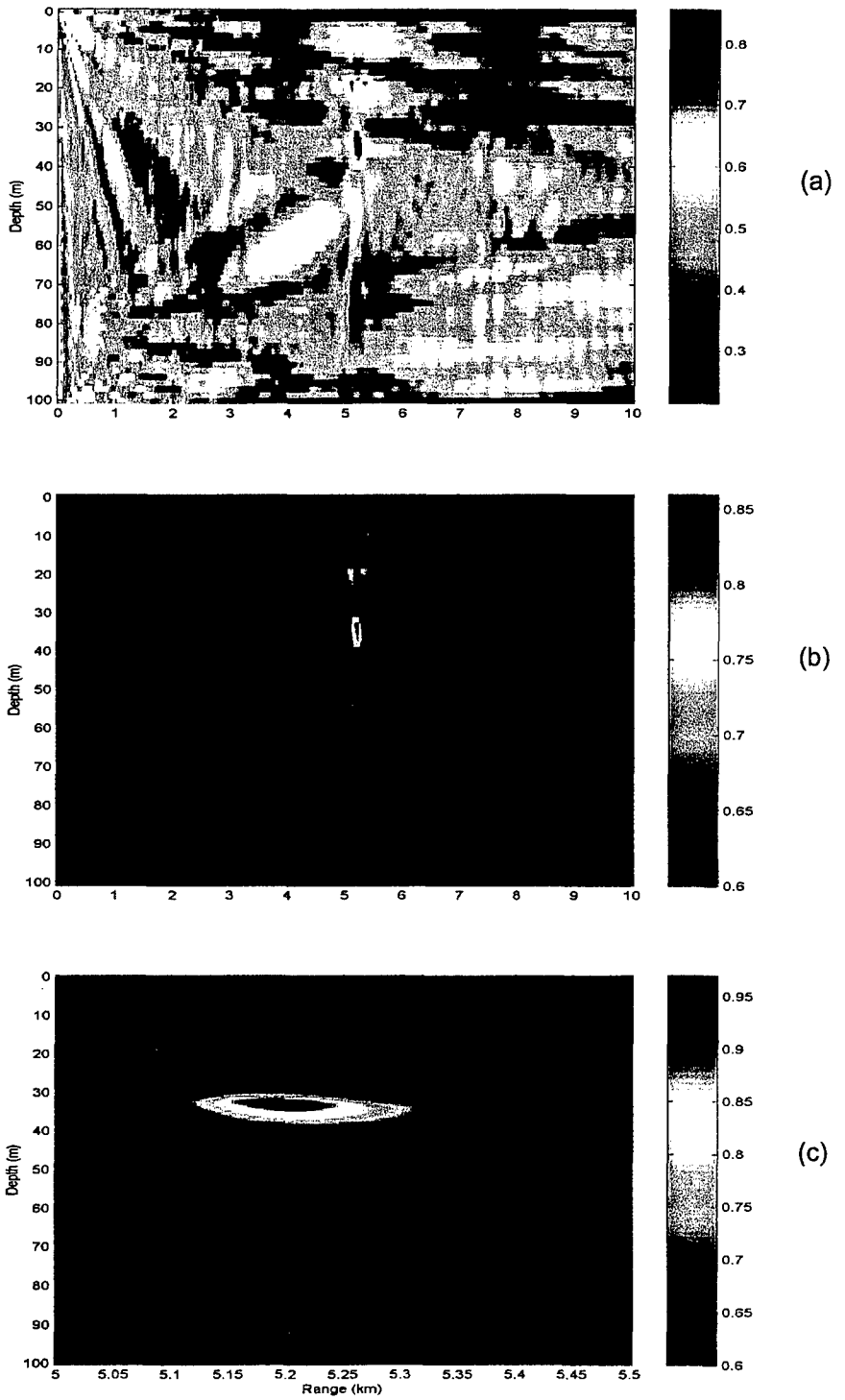

Figure 4.1: For Case 1, the ambiguity surfaces for the IFACM algorithm for the shallow array in an all-known environment: (a) the full range search area and the full dynamic range; (b) the full range search area with an adjusted dynamic range; (c) the 'zoomed-in' ambiguity surface with an adjusted dynamic range.

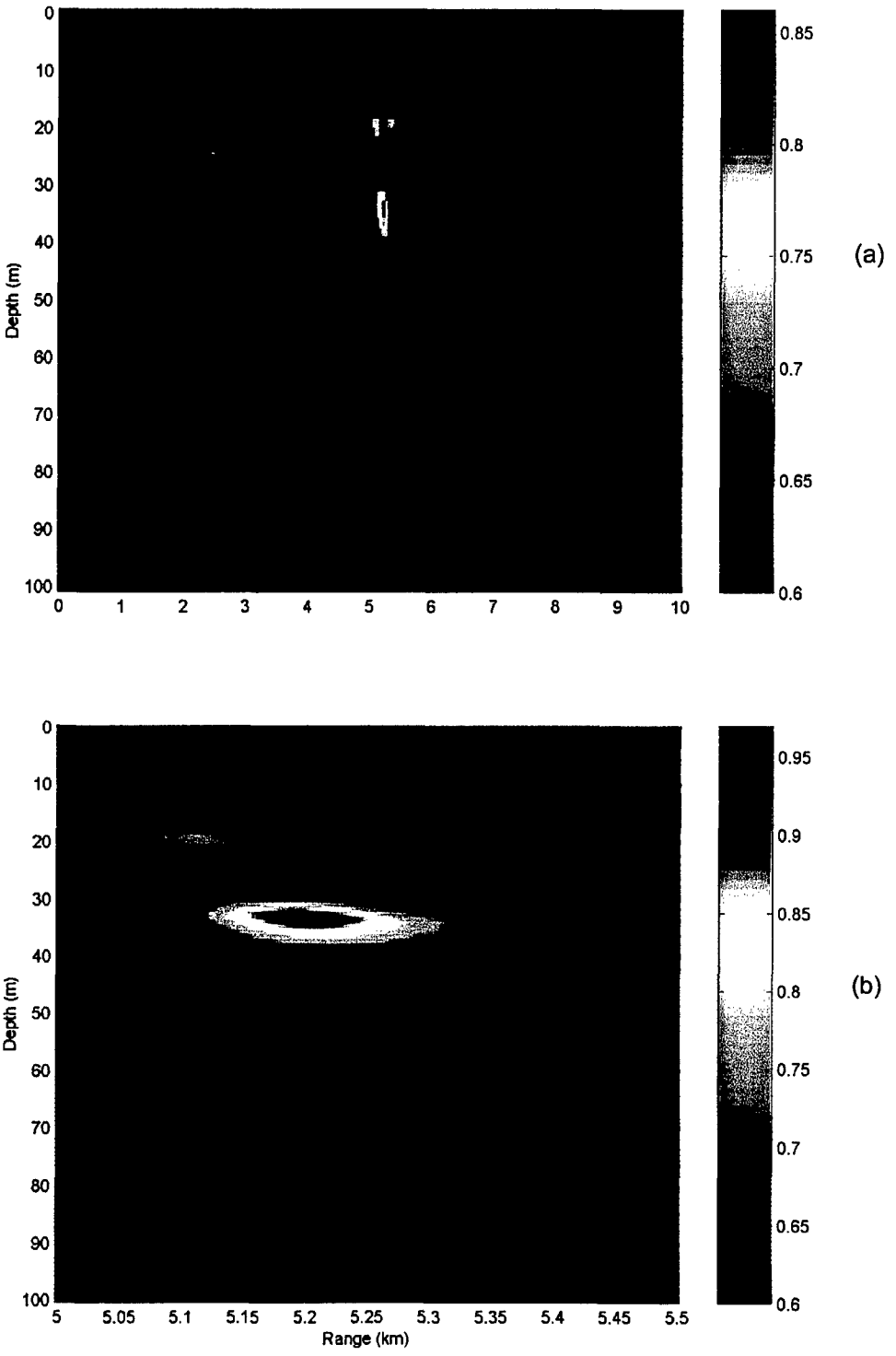

Figure 4.2: For Case 1, the ambiguity surfaces for the KzFACM algorithm for the shallow array in an all-known environment: (a) the full range search area; (b) the 'zoomed-in' ambiguity surface.

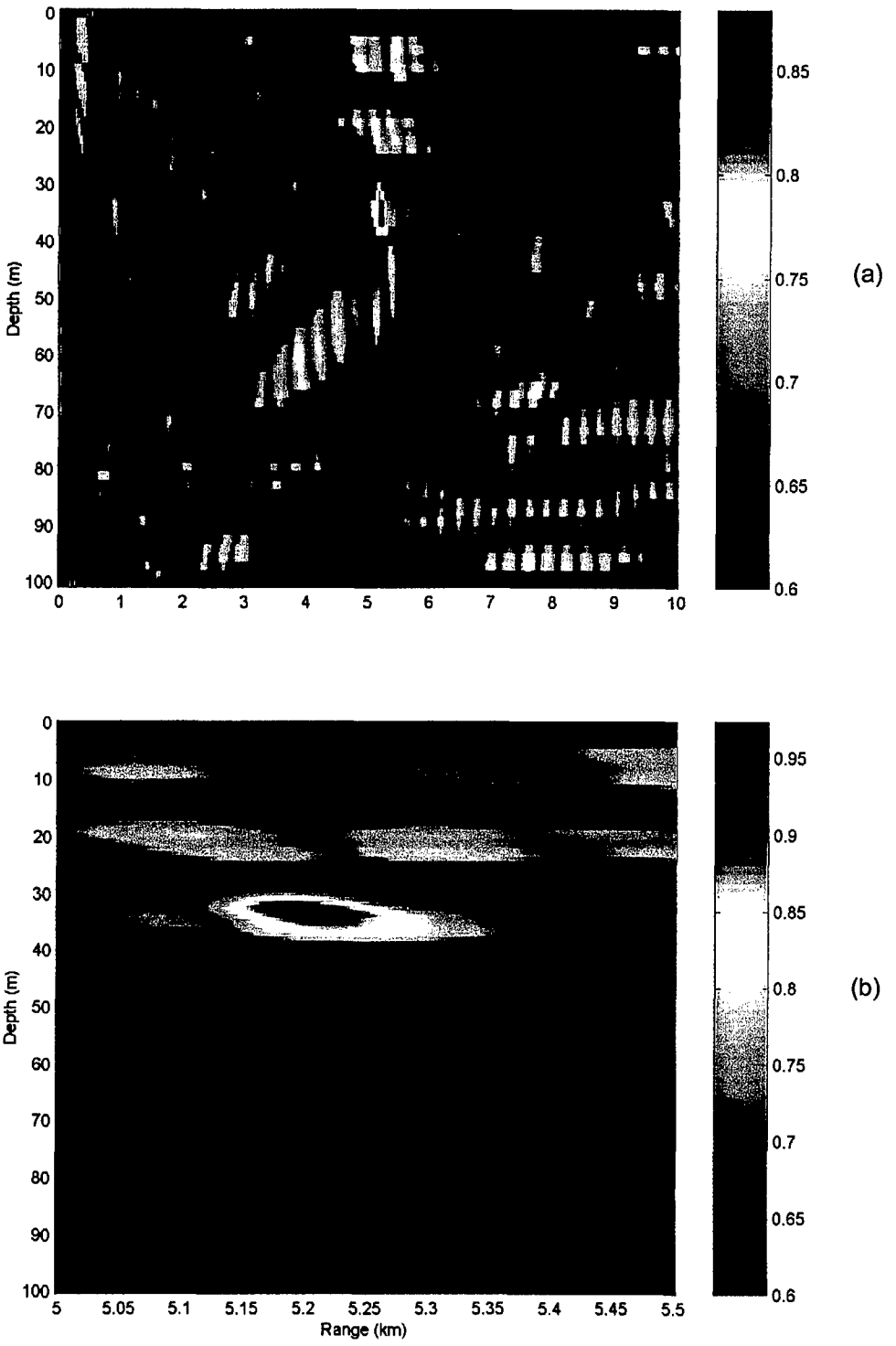

Figure 4.3: For Case 1, the ambiguity surfaces for the ZFACM algorithm for the shallow array in an all-known environment: (a) the full range search area; (b) the 'zoomed-in' ambiguity surface.

Observing Figs. 4.1 through 4.3 the following remarks can be made. For all three algorithms the maximum value of the autocorrelation matching function occurs at the correct source location: 5.2 km and 33 m deep. Comparing the full range search areas, the IFACM and KzFACM results show a very good match and also a close resemblance. The ZFACM result shows a good match with stronger sidelobes. The footprints for IFACM and KzFACM are almost equal in shape and size, where ZFACM's footprint is larger in depth and range.

Comparing the 'zoomed-in' versions shows a similar outcome. The IFACM and KzFACM results have a close resemblance and on both ambiguity surfaces almost no sidelobes are present. Again, their footprints are practically the same. The ZFACM result has more sidelobes of medium-high magnitude in the vicinity of the actual source location. Also, ZFACM's footprint is smaller in range but larger in depth.

In Fig. 4.4 the ambiguity surfaces are shown for the deep array. For all three algorithms the 'zoomed-in' surfaces with adjusted dynamic range are displayed. With regards to this figure the following remarks can be made. For all three algorithms the maximum value of the autocorrelation matching function is at the correct source location. Again, the IFACM and KzFACM results show a very good match and also a close resemblance. No other sidelobes are present on these ambiguity surfaces. The ZFACM result is a good match with only one sidelobe of medium-high magnitude directly under the source location. The footprints for IFACM and KzFACM are nearly the same, where ZFACM's footprint is marginally larger in depth.

Comparing these 'zoomed-in' versions for the deep array with the 'zoomed-in' ambiguity surfaces for the shallow array (Figs. 4.1(c), 4.2(b) and 4.3(b)), the following can be observed. For all three algorithms, the match for the deep array is better than for the shallow array, since fewer sidelobes of medium magnitudes are present. Especially the ZFACM match has improved. Also for all algorithms the deep array footprints are (marginally) smaller in range and twice as small in depth.

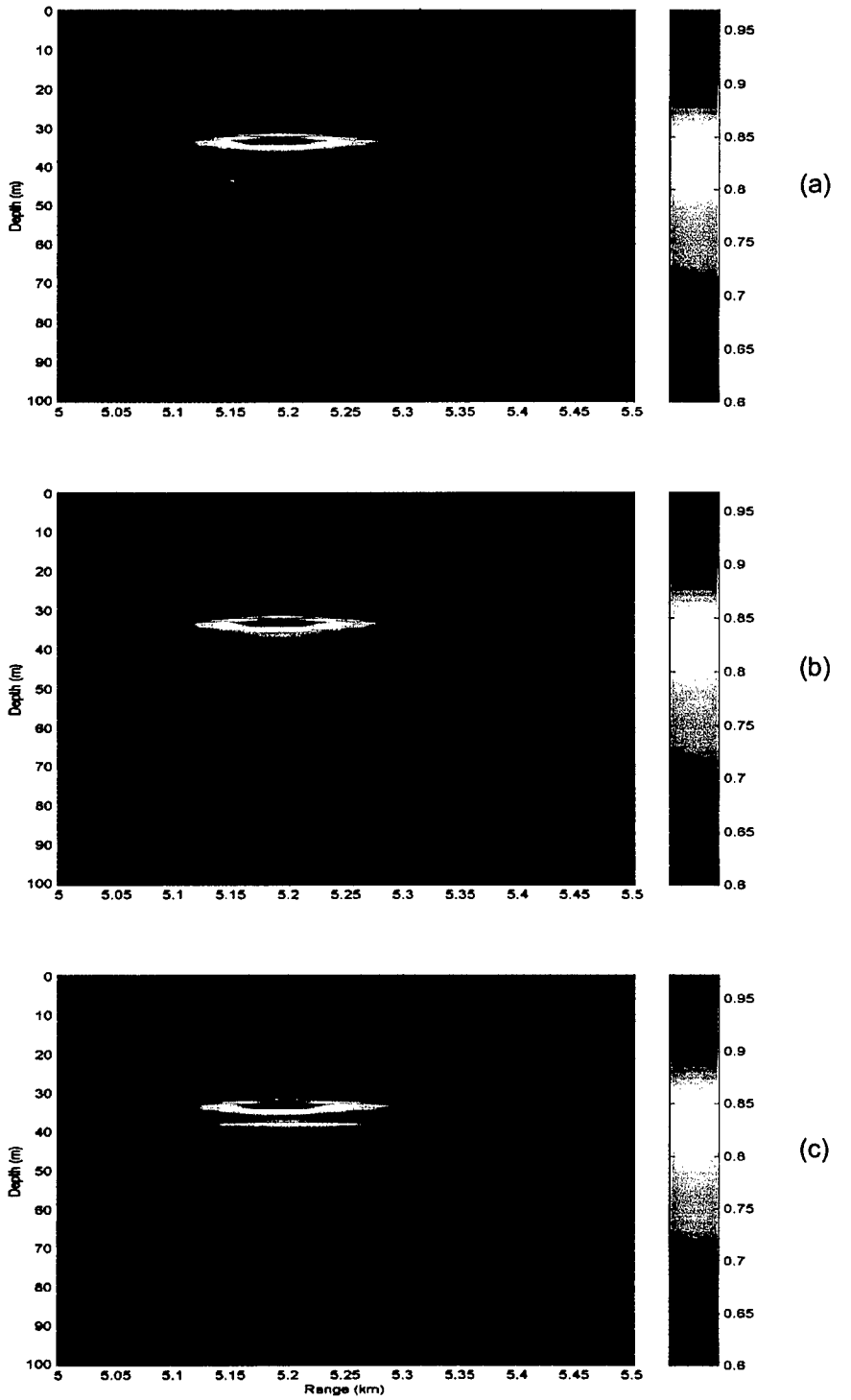

Figure 4.4: For Case 1, the 'zoomed-in' ambiguity surfaces for the deep array in an all known environment: (a) the IFACM algorithm; (b) the KzFACM algorithm; (c) the ZFACM algorithm.

This performance difference between the two arrays may be explained as follows. For an isospeed environment, an array closest to the middle of the water column will intercept more multipath structure than an array further away from the middle. In this experiment, the water column is 100 m deep. The deep array is roughly located at a depth of 55 m, which is nearly halfway in the water column.

The shallow array, on the other hand, is roughly located at a depth of 20 m, which is approximately at 1/5 of the water column. The central position in the water column of the deep array will make more interception of multipath structure possible, resulting in a better performance than the shallow array.

Recalling the fact that Case 1 is the theoretical case where transient and replica signals are 100% the same, one would expect the maximum value of the autocorrelation matching algorithms to be unity. However, this is not the case, as can be seen in these first ambiguity surfaces. The most likely factor causing this is the discrepancy between the source location and the grid point locations. The setup of the experiment is chosen in such a way that all receiver locations, range and depth, exactly coincide with the grid point locations. For the source locations, the source range usually coincides with grid point range locations. However, the source depth seldom coincides with the grid point depth locations. This small source location error will contribute to the autocorrelation value error. Also, at a smaller scale, round-off errors will contribute to the autocorrelation value error.

B. CASE 2: POSITIVE SSP GRADIENT

In Case 2, the source was located at a range of 4.6 km from the vertical line array and at a depth of 27 m. The sound speed was range-independent with a positive, linear gradient (upward refracting) sound speed profile of 1497 m/s at the surface and 1499 m/s at a depth of 100 m. The density of water was

assumed to be 1.0 g/cm^3. The bottom was chosen to be a somewhat 'bumpy' bottom with the following depths: 100 m at 0 km; 102 m at 2.5 km; 99 m at 5 km; 100 m at 7.5 km; and 102 m at 10 km. Its compressional sound speed was 1595 m/s, the density 1.52 g/cm^3, and the attenuation 0.11 dB/km/Hz.

In this case, three different environmental situations are considered. For the first situation, the environment is completely known and the transient and replica field functions, determined by the MMPE propagation model, have exactly the same input parameters. In other words, there is no environmental mismatch. Figure 4.5 shows the ambiguity surfaces for the shallow array for all three algorithms.

Observing this figure the following remarks can be made. For all three algorithms the maximum value of the autocorrelation matching function occurs at the correct source location: 4.6 km and 27 m deep. All three algorithms show a close resemblance, since the sidelobes occur at exactly the same locations. The difference between the results is mostly evident in the magnitude of the sidelobes and marginally in the peak values. The IFACM and KzFACM results show a good match, since only sidelobes of medium-low magnitudes occur on the ambiguity surface. The ZFACM result is a moderate match, because more sidelobes of medium-high magnitudes are displayed. For all three algorithms these sidelobes mainly occur behind the source location (seen from the vertical line array), acting like 'shadows'. The footprints are the same in range for all three algorithms, although ZFACM's footprint is marginally larger in depth.

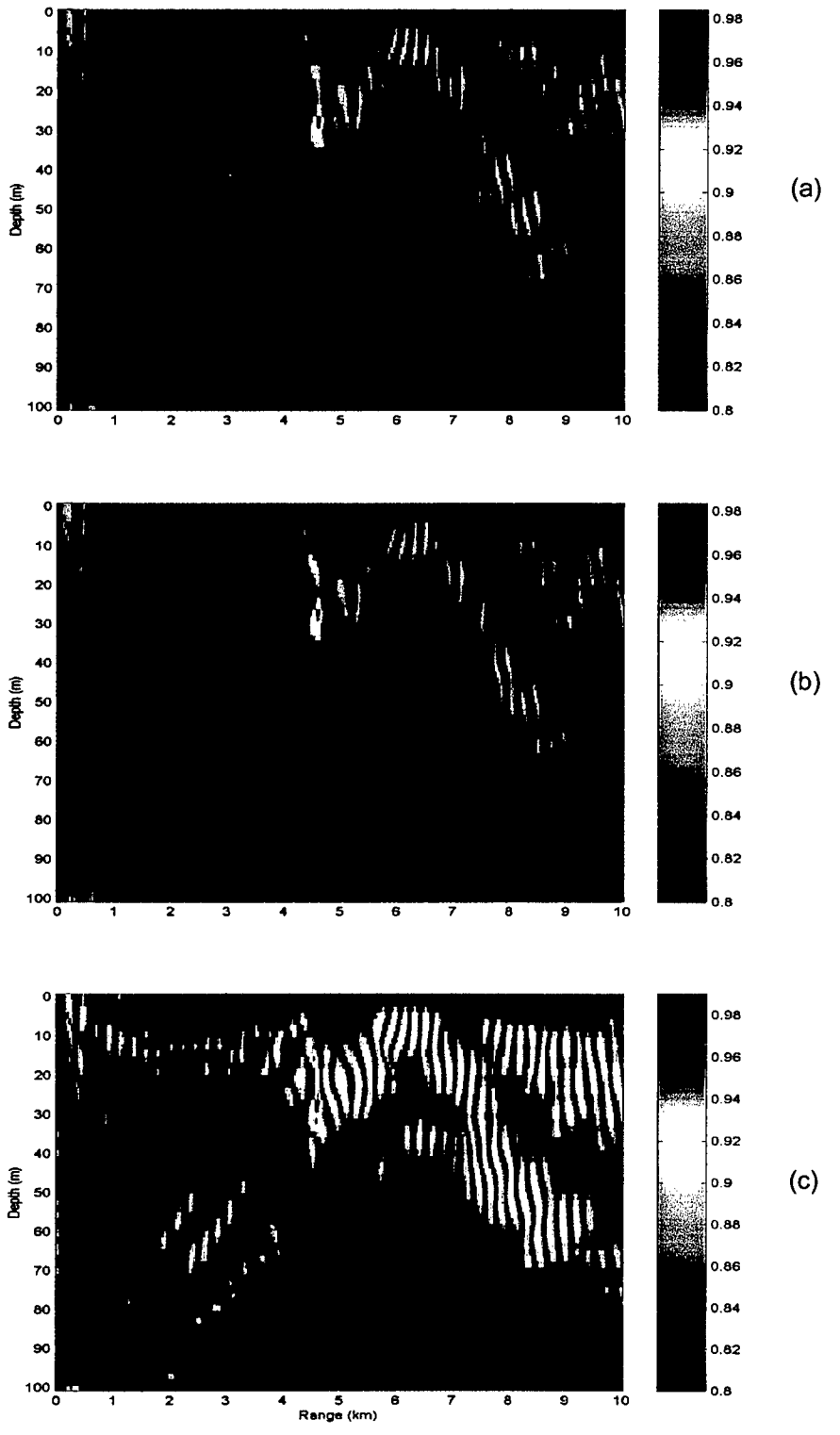

Figure 4.5: For Case 2, the ambiguity surfaces for the shallow array with no environmental mismatch: (a) the IFACM algorithm; (b) the KzFACM algorithm; (c) the ZFACM algorithm results.

Comparing the shallow array results of Case 2 with the shallow array results of Case 1 (Figs. 4.1(b), 4.2(a) and 4.3(a)), the following can be observed. Although in each case the transient and the replica signals were 100% the same, an isospeed environment (Case 1) seems to provide a better match for all three algorithms than a positive SSP environment (Case 2). The footprint sizes are approximately the same. However, in Case 2 more sidelobes of high magnitudes are present in the search area. This difference may be explained as follows. For an isospeed environment, no ray-bending will take place, versus the upward refracting rays for a positive sound speed gradient environment. If the rays do not bend, an array can intercept multipaths that have traveled through any depth of the water column. For upward refracting rays, an array can only intercept multipaths that have traveled through the shallower part of the water column. This implies that for the shallow array more multipath interception can take place when the rays do not bend, e.g., in the isospeed environment, and the localization peak is more unique. In the upward refracting case, the results are less unique, giving rise to more sidelobe structure.

For the same environmental conditions for both the transient and the replicas, Figs. 4.6 through 4.8 display the results for the deep array for all three algorithms. For the IFACM and the KzFACM algorithm the 'zoomed-in' ambiguity surfaces are also shown.

Regarding these figures the following observations can be made. Concerning the full range search area, the maximum value of the autocorrelation matching function for all three algorithms occurs at the correct source location. Also, all three results show a very good match and a close resemblance. The IFACM and KzFACM results show only small sidelobes of medium-high magnitude directly next to the footprint. The ZFACM result shows at this same location only a slightly larger sidelobe with similar value. The footprints are roughly equal in size. Comparing the 'zoomed-in' results for IFACM and

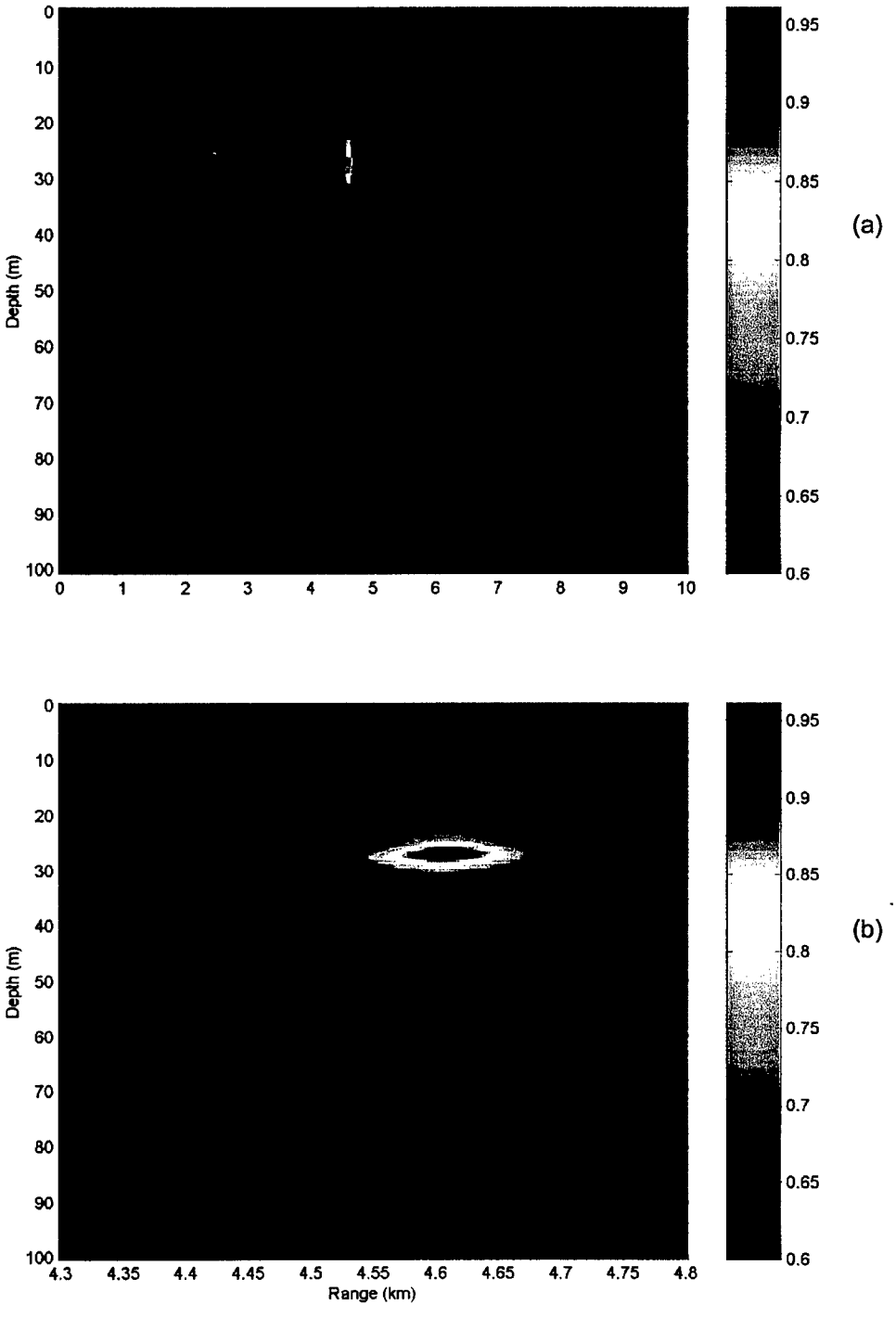

Figure 4.6: For Case 2, the ambiguity surface for the IFACM algorithm for the deep array with no environmental mismatch: (a) the full range search area; (b) the 'zoomed-in' version.

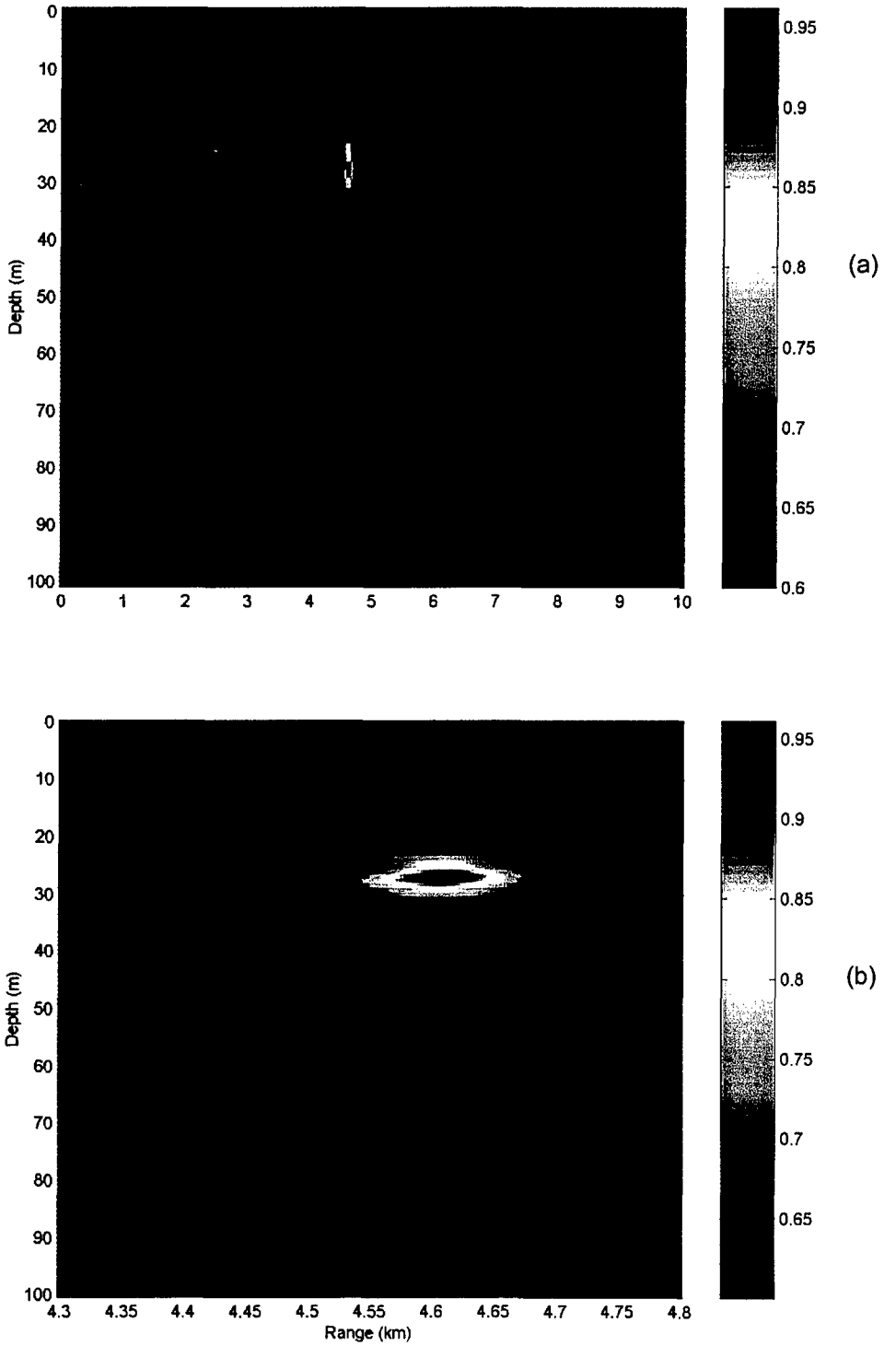

Figure 4.7: For Case 2, the ambiguity surface for the KzFACM algorithm for the deep array with no environmental mismatch: (a) the full range search area; (b) the 'zoomed-in' ambiguity surface.

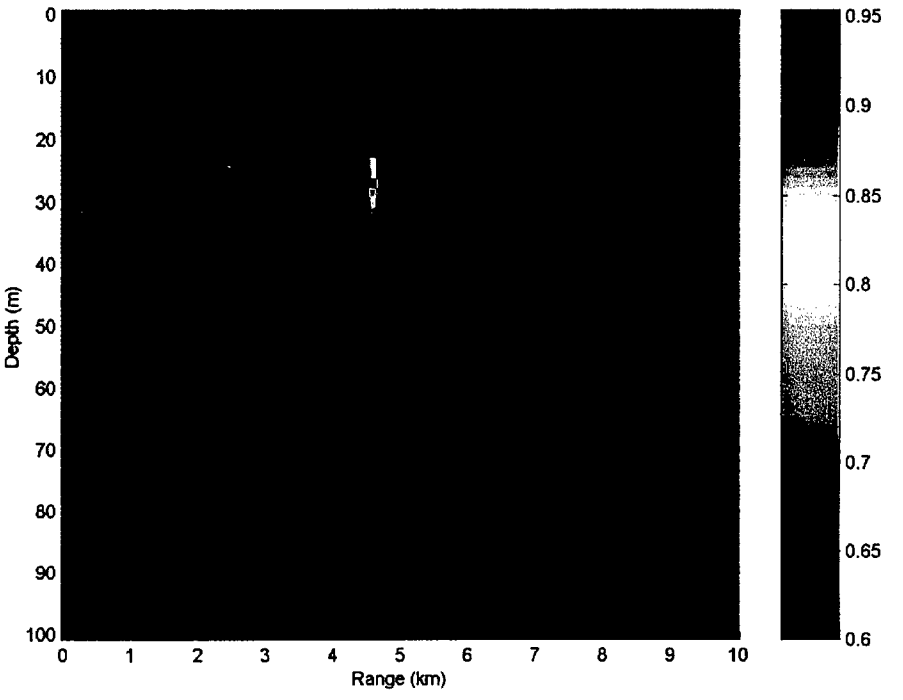

Figure 4.8: For Case 2, the full range ambiguity surface for the ZFACM algorithm for the deep array with no environmental mismatch.

KzFACM shows the same footprint size, although KzFACM has more areas with medium magnitude sidelobes surrounding the footprint.

Comparing the full range search area results for the deep array with the shallow array results for Case 2 (Fig. 4.5), the following can be noted. In both cases the maximum occurs at the correct source location. For all three algorithms, the match for the deep array is better than for the shallow array, since fewer sidelobes are showing in the search area. The footprint size is approximately the same for all algorithms for both arrays. This difference is consistent with previous comments. In an environment with a positive sound speed gradient, more upward refracting rays can be intercepted by a deep array than by a shallow array, providing a more unique localization.

At this point an important observation can been made. From the previous thesis work, a major result was that FACM was a more robust algorithm than TACM. This means that for these algorithms the actual envelope matching in the time-domain leads to a better result. Using this same argument, the algorithms developed for this thesis can be compared. For all algorithms one parameter of the envelope matching is the time-domain. The other parameter is either in the depth-domain (for KzFACM), or in the wavenumber-domain (for ZFACM). For all three cases the resemblance of the results is remarkable. Sidelobes occur at nearly the same location. Any differences in results mainly concern sidelobe magnitudes and relative peak-to-sidelobe ratios. This suggests that for these autocorrelation matching algorithms, the time-domain component of the envelopes is the dominant factor.

The second situation for Case 2 contains an environmental mismatch in the sound speed profile. The exact bottom profile and all other input parameters are known.

In a real life scenario, the received transient signal would have the correct sound speed profile and the predictions (the replicas) would have the incorrect one, resulting in an environmental mismatch. In order to reduce the computational load, the mismatch is implemented in the transient signal, leaving the replicas unchanged. While this is not exactly a reciprocal change for the ambiguity surface, the level of performance degradation is expected to be the same.

The sound speed profile mismatch is an assumed isospeed profile of 1498 m/s versus the actual positive sound speed gradient of 1497 m/s at the surface and 1499 m/s at a depth of 100 m. Thus, the mismatch is a depth average of the "true" profile.

Figures 4.9 through 4.11 show the ambiguity surfaces for the three algorithms for the shallow array. For the IFACM and the KzACM algorithms, the 'zoomed-in' versions are shown as well.

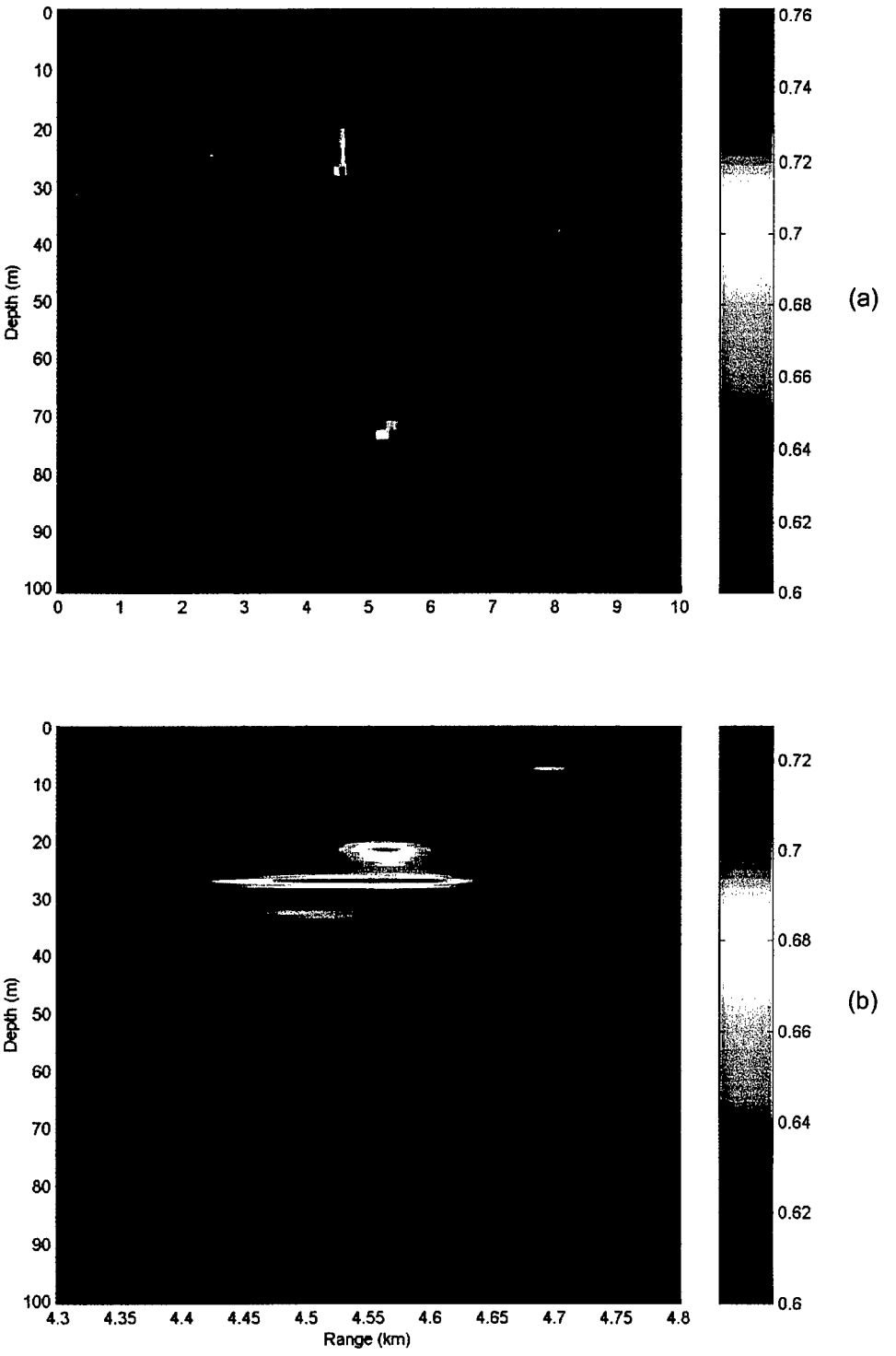

Figure 4.9: For Case 2, the ambiguity surfaces for the IFACM algorithm for the shallow array in a SSP mismatch situation: (a) the full range search area; (b) the 'zoomed-in' ambiguity surface.

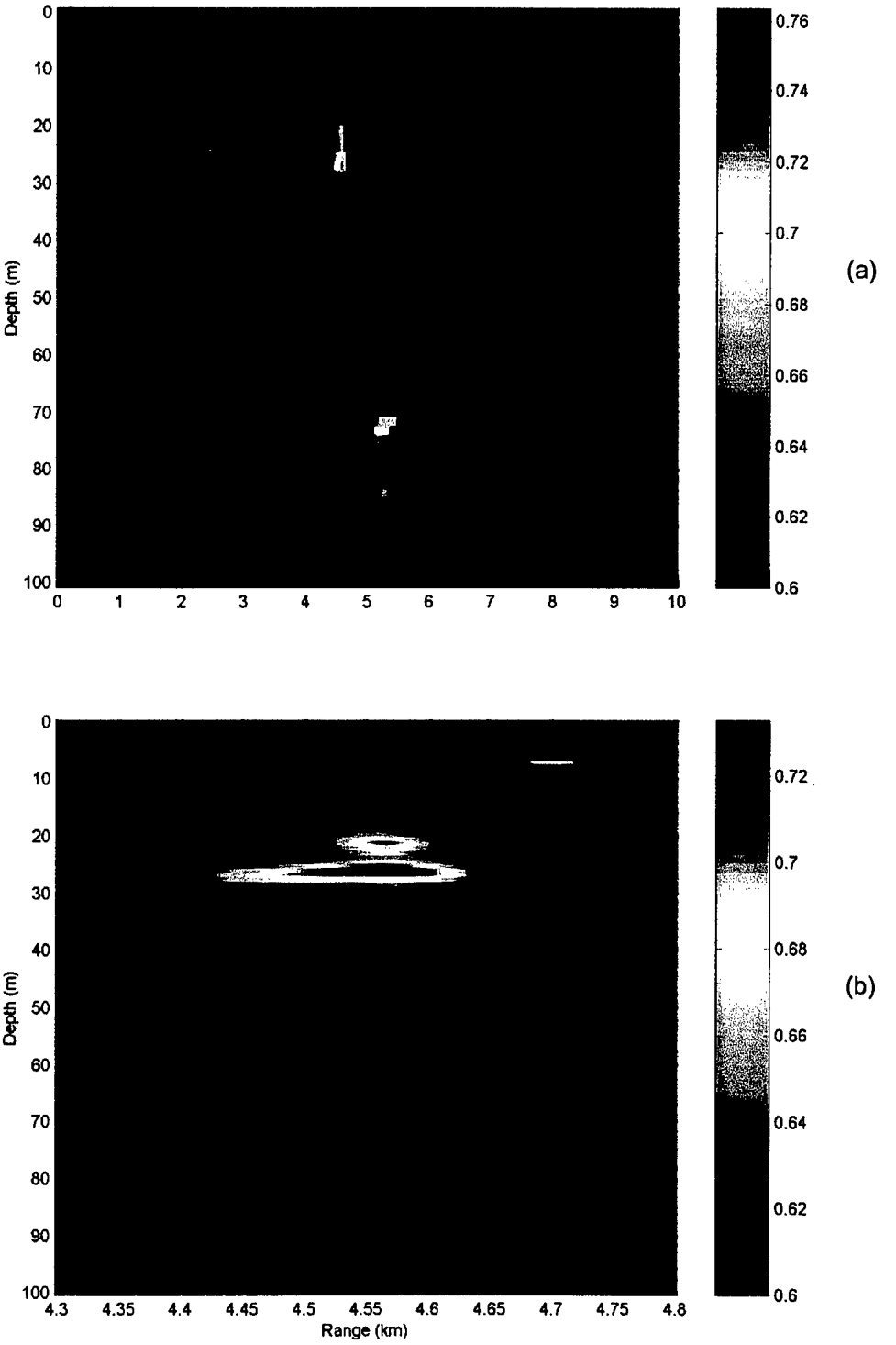

Figure 4.10: For Case 2, the ambiguity surfaces for the KzFACM algorithm for the shallow array in a SSP mismatch situation: (a) the full range search area; (b) the 'zoomed-in' version.

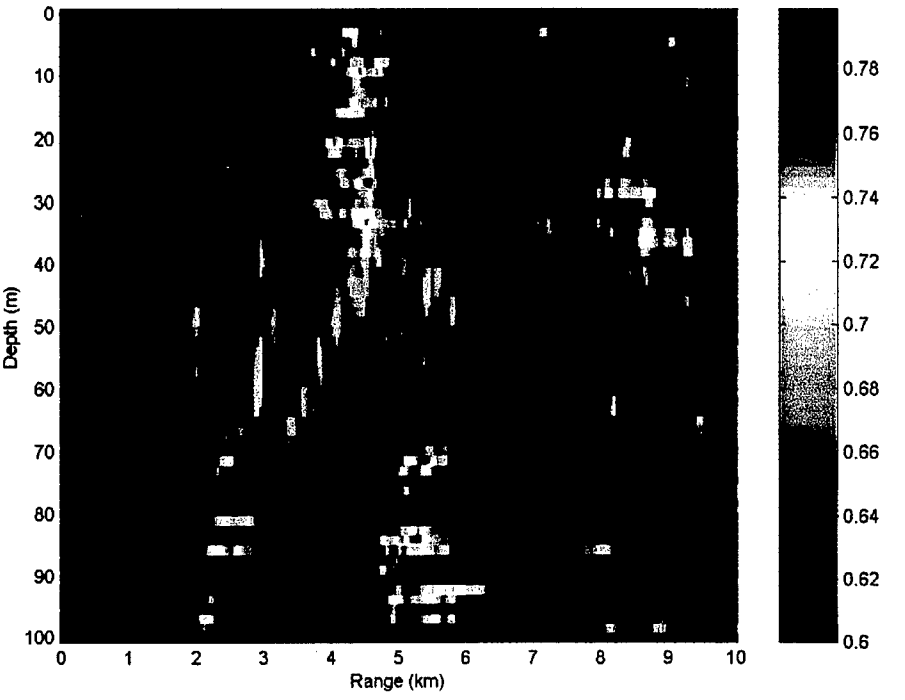

Figure 4.11: For Case 2, the full range ambiguity surface for the ZFACM algorithm for the shallow array in a SSP mismatch situation.

Observing Figs. 4.9 through 4.11 the following remarks can be made. Concerning the full range search area, for all three algorithms the maximum value of the autocorrelation matching function does not occur at the source location. The calculated source location is approximately 40 m closer in range and 1.5 m shallower in depth than the actual location. Besides that, the IFACM and KzFACM results show a very good match and a close resemblance. Only one small sidelobe is present in the search area, and the footprint size is very small. The ZFACM result is a moderate match. A number of sidelobes of high- and medium-high magnitudes are present on the ambiguity surface, and the footprint size is twice as large in range compared to the IFACM and KzFACM footprints. Comparing the 'zoomed-in' results of IFACM and KzFACM displays more clearly the source location mismatch. Also, the footprint shapes show some difference. The IFACM footprint is larger in range, but smaller in depth.

Comparing the shallow array results for Case 2 with and without the SSP mismatch (Figs. 4.5 and 4.9-11), the following can be noted. For all three algorithms, the maximum values in the ambiguity surfaces for the SSP mismatch situation are significantly lower (not above 0.8) than without mismatch. However, for the IFACM and KzFACM algorithms, fewer sidelobes of medium- low magnitude appear in the SSP mismatch situation than without mismatch. Therefore, remarkably, the match appears to be better with a SSP mismatch than without. The footprint sizes are roughly the same for both algorithms in both situations. The ZFACM algorithm match is less with the SSP mismatch than without mismatch. Although more 'shadows' appear without mismatch, they look less scattered and have a smaller relative value than with the SSP mismatch. Also, the ZFACM footprint is smaller without mismatch than with the SSP mismatch.

Figures 4.12 through 4.14 show the ambiguity surfaces for the three algorithms for the deep array. Again, for the IFACM and the KzACM algorithms, the 'zoomed-in' versions are shown also.

Regarding these figures the following observations can be made. Concerning the full range search area, for all three algorithms the maximum value of the autocorrelation matching function clearly does not occur at the source location. The maximum value of the autocorrelation matching function is approximately at a range and depth of 8.7 km and 26 m, respectively, where the actual source location is at a range of 4.6 km and at a depth of 27 m. Since numerous sidelobes are present in the search areas, none of them being close to the actual source location, a discussion about footprint sizes is not very meaningful. The 'zoomed-in' results of IFACM and KzFACM show a possible match with a close resemblance between these two results. Within the selected window, the calculated source location has no range mismatch but there is a 7 m mismatch (shallower than actual) in depth. However, this 'zoomed-in' result is very unlikely to be found, assuming that 'zooming-in' normally is the next

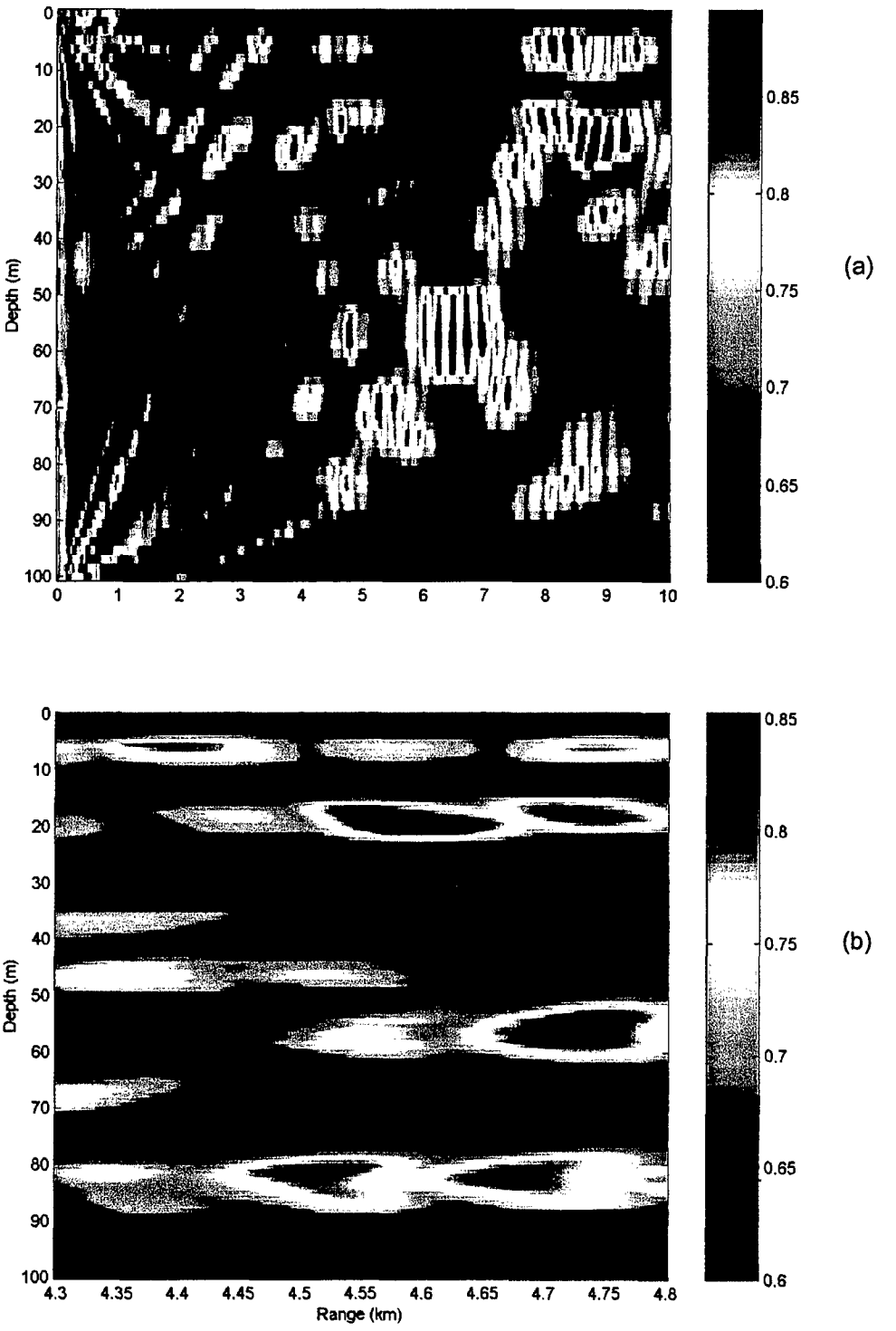

Figure 4.12: For Case 2, the ambiguity surfaces for the IFACM algorithm for the deep array in a SSP mismatch situation: (a) the full range ambiguity surface; (b) the 'zoomed-in' surface.

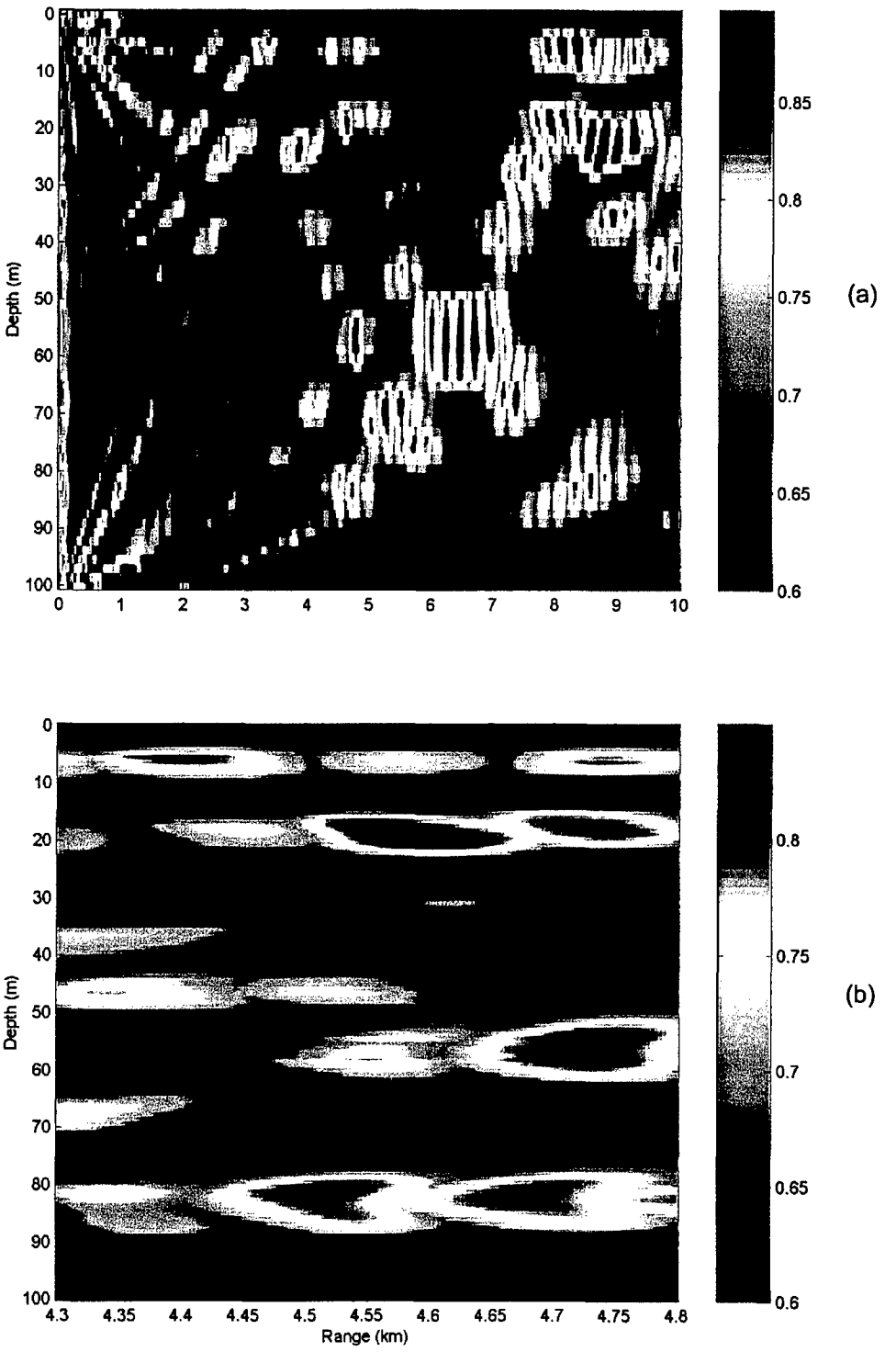

Figure 4.13: For Case 2, the ambiguity surfaces for the KzFACM algorithm for the deep array in a SSP mismatch situation: (a) the full range search area; (b) the 'zoomed-in' ambiguity surface.

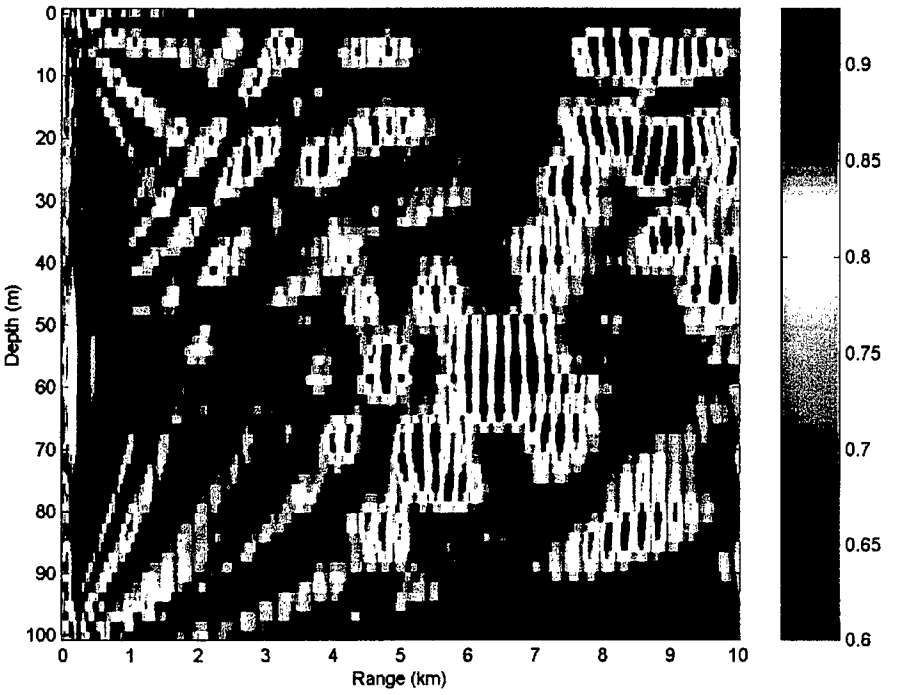

Figure 4.14: For Case 2, the full range ambiguity surface for the ZFACM algorithm for the deep array in a SSP mismatch situation.

stage after 'full range searching'. Initially observing the full range search area, a 'zoomed-in' window would be placed around displayed maximum values. In this case that would mean that the window would be placed outside the actual source location, therefore the correct source location would never be found. The fact that a possible match has been found in the 'zoomed-in' search area is purely based on coincidence, and on the settings of the scenarios. The moderate footprint size, approximately 100 m in range and 5 m in depth, emphasizes the misleading nature of these results.

The most likely reason for this complete mismatch by all three algorithms is the fact that in this upward refracting environment the deep array could be located in a shadow zone. These shadow zones are dependent on source range and depth, and any target located in such a zone is practicably 'invisible'.

The very close resemblance between the three results is again remarkable. As stated earlier, the depth- or wavenumber-component is of much lesser importance than the time-component in the envelope matching technique of these autocorrelation matching algorithms. Apparently this is even the case when the match fails completely.

The last situation for Case 2 contains an environmental mismatch in the bottom bathymetry. This time, the sound speed profile and all other input parameters are known. The bottom bathymetry mismatch is an assumed flat bottom at a depth of 100 m versus the actual bottom.

Again, in order to reduce the computational load, the mismatch is implemented in the transient signal, leaving the replicas unchanged. Figure 4.15 shows the ambiguity surfaces for the three algorithms for the shallow array, while Fig. 4.16 displays the results for the deep array.

Observing Fig. 4.15 the following remarks can be made. For all three algorithms the maximum value of the autocorrelation matching function occurs at a range of 4.72 km and a depth of 27 m. The actual source location is 4.6 km and 27 m deep, resulting in a range mismatch of 120 m and a perfect match in depth. All three algorithm results show a close resemblance and a reasonable match with the ZFACM result having sidelobes of slightly higher magnitudes. All results show many sidelobes. For the IFACM and the KzFACM results these sidelobes have medium magnitudes in front of the source location, and appear as medium-high magnitude 'shadows' behind the source location. For the ZFACM result these sidelobes have medium-high magnitudes in front of the source location and the 'shadows' behind the source location are 'red-valued'. The footprints for the IFACM and KzFACM results are equally shaped and have a moderate size. The footprint for the ZFACM result, however, is nearly twice as large in depth.

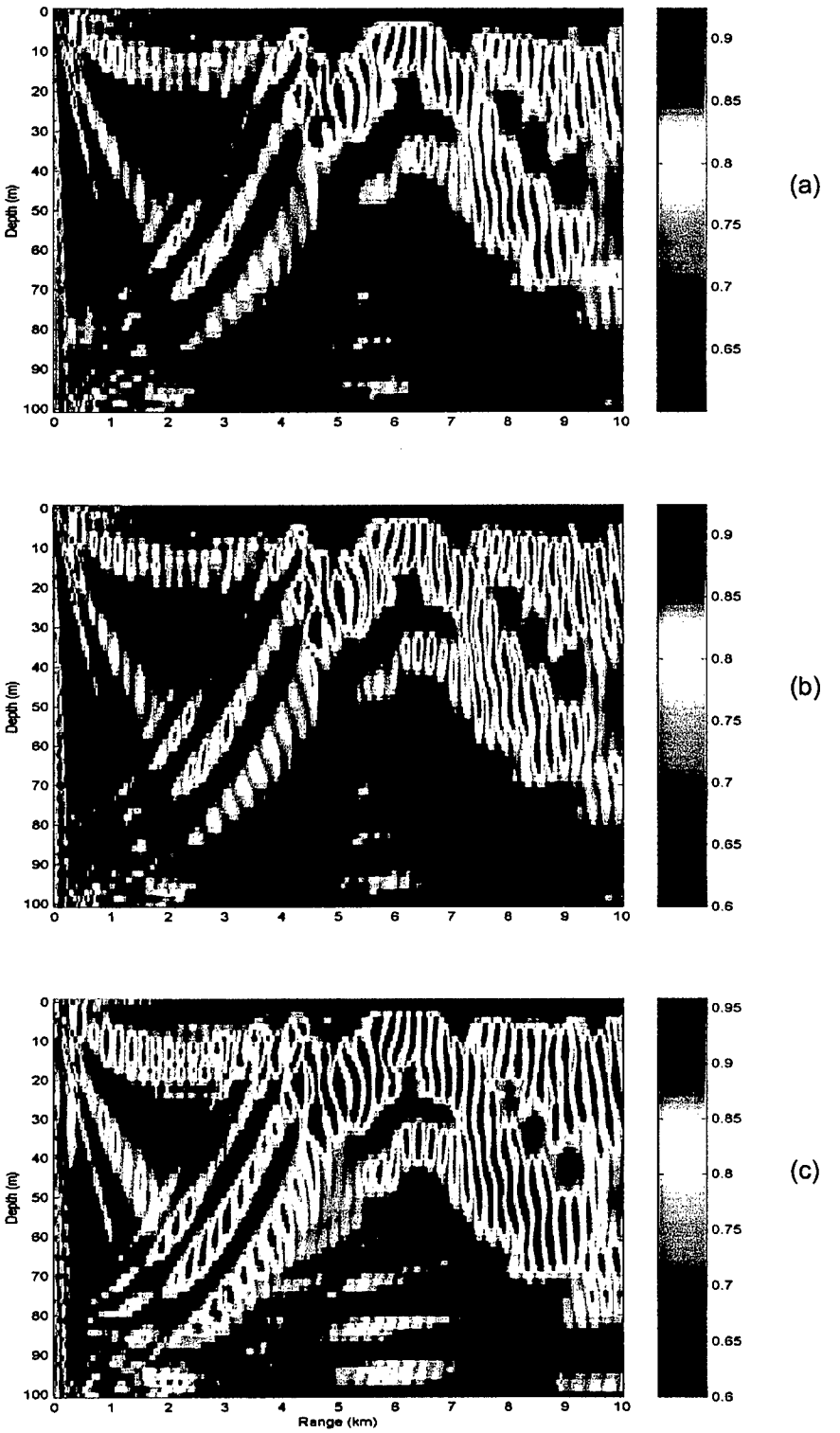

Figure 4.15: For Case 2, the ambiguity surfaces for the shallow array in a bottom bathymetry mismatch situation: (a) the IFACM algorithm; (b) the KzFACM algorithm; (c) the ZFACM algorithm.

Comparing these shallow array results with the shallow array results with no environmental mismatch (Fig. 4.5), the following can be noted. First of all, the source location is mismatched in range in the bottom bathymetry mismatch situation versus a perfect location match without mismatch. Furthermore, as one might expect, without mismatch the results give a better match than the results with the bottom bathymetry mismatch. Note that the ambiguity surfaces for all three algorithms for both situations show the same pattern. Even for different mismatch situations there is resemblance between all the results. However, with the bottom bathymetry mismatch more sidelobes and 'shadows' of high magnitudes are present. Also, the footprint size for this mismatch situation is at least twice as large.

Regarding the deep array results in Fig. 4.16 the following observations can be made. For all three algorithms the maximum value of the autocorrelation matching function occurs at a range of 4.72 km and a depth of 27 m, where the actual source location is 4.6 km and 27 m deep. So, like the shallow array, this results in a range mismatch of 120 m and a perfect match in depth. All three algorithms show a remarkably good match. Note that dynamic range has been adjusted downwards to show some sidelobes in the search area. Footprint sizes for all three are very small, although the ZFACM result shows more areas with medium magnitude around the calculated source location.

Comparing these deep array results with the shallow array results for the same mismatch situation (Fig. 4.15), the following can be noted. For both arrays the source location mismatch, which is only a range mismatch, is the same. The deep array gives a much better match for all algorithms. Practically no sidelobes are present on the deep array ambiguity surfaces, where the shallow array ambiguity surfaces are full of sidelobes of medium-high magnitudes and 'shadows' of high magnitudes. Footprint sizes are at least four times larger for the shallow array results.

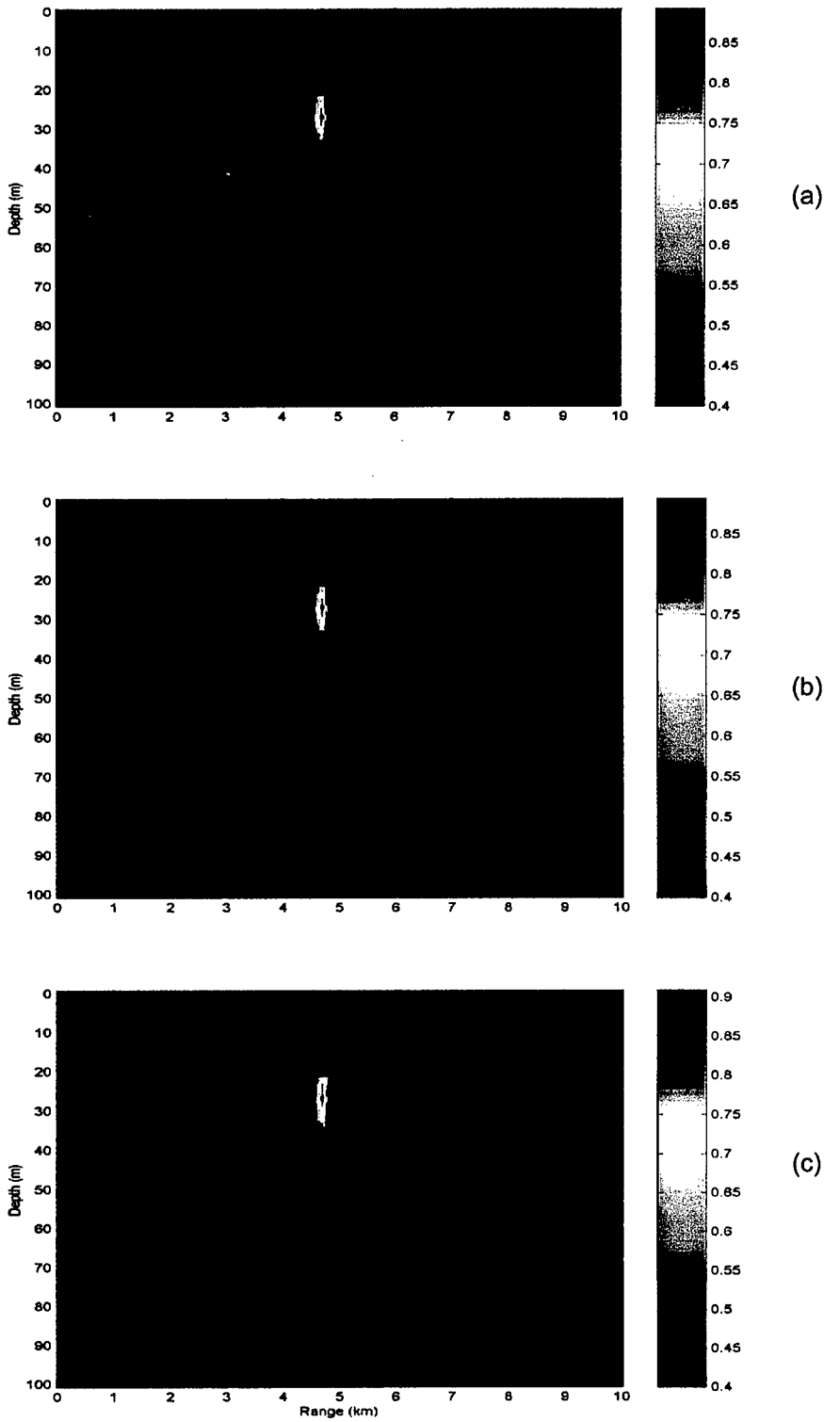

Figure 4.16: For Case 2, the ambiguity surfaces for the deep array in a bottom bathymetry mismatch situation: (a) the IFACM algorithm; (b) the KzFACM algorithm; (c) the ZFACM algorithm.

Comparing the deep array results with the deep array results without environmental mismatch (Fig. 4.6), the following can be observed. First of all, with the bottom bathymetry mismatch the source location has a slight range mismatch. Furthermore, in both situations the results of all three algorithms give a very good match. The ambiguity surfaces show no sidelobes, and the footprint sizes are very small. Apparently the deep array in a positive sound speed environment is weakly sensitive to bottom bathymetry mismatch situations, which could have been expected. Still, both shallow and deep array results did produce a range mismatch in the presence of the bathymetry mismatch, indicating some sensitivity.

C. CASE 3: STRONG NEGATIVE SSP GRADIENT

For this case the source was located at a range of 7.2 km from the vertical line array and at a depth of 31 m. The sound speed was range-independent with a strong negative, bi-linear gradient (downward refracting) sound speed profile of 1528 m/s at the surface, 1510 m/s at a depth of 50 m, and 1489 m/s at a depth of 100 m. The density of water was assumed to be 1.0 g/cm^3. The bottom was chosen to be a 'bumpy' bottom with the following depths: 102 m at 0 km; 101 m at 2.5 km; 99 m at 5 km; 102 m at 7.5 km; and 99 m at 10 km. Its compressional sound speed was 1604 m/s, the density 1.47 g/cm^3, and the attenuation 0.12 dB/km/Hz.

Like the previous case, three different environmental situations are considered for Case 3. For the first situation, the environment is completely known and the transient and replica field functions have exactly the same input parameters. In other words, there is no environmental mismatch. Figure 4.17 shows the ambiguity surfaces for the shallow array for all three algorithms. Figure 4.18 displays the results for the deep array for all three algorithms.

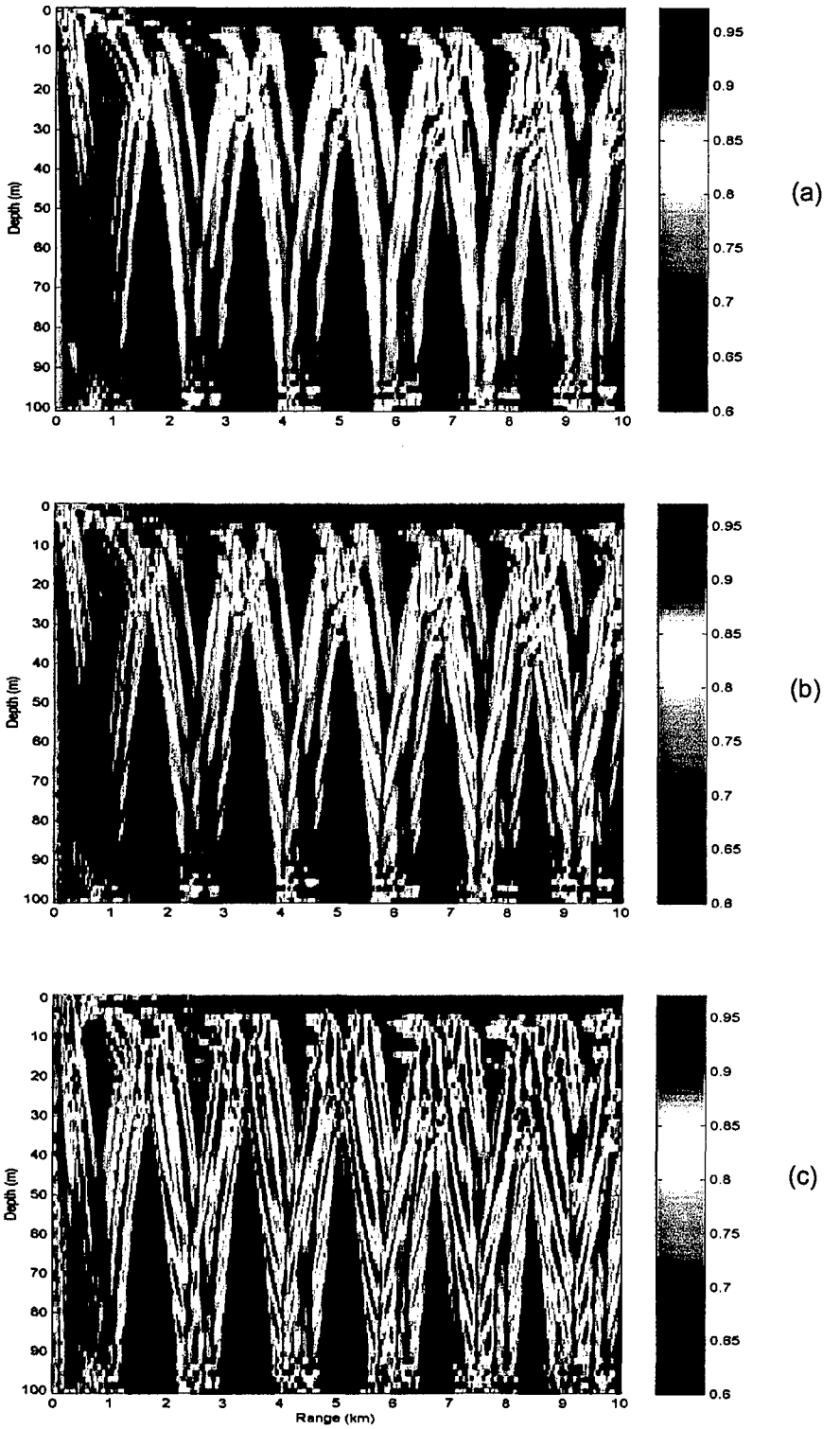

Figure 4.17: For Case 3, the ambiguity surfaces for the shallow array with no environmental mismatch: (a) the IFACM algorithm; (b) the KzFACM algorithm; (c) the ZFACM algorithm.

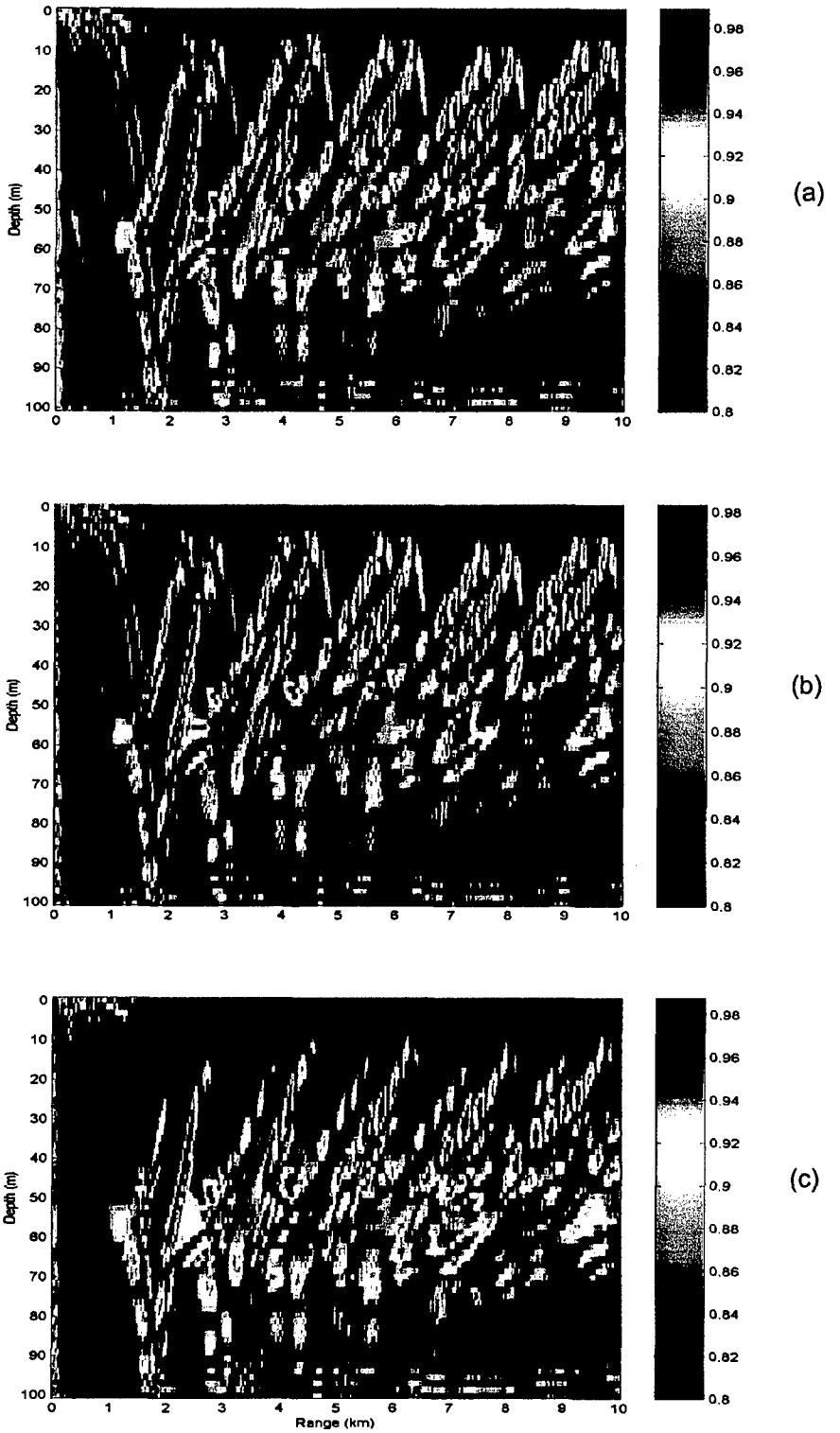

Figure 4.18: For Case 3, the ambiguity surfaces for the deep array with no environmental mismatch: (a) the IFACM algorithm; (b) the KzFACM algorithm; (c) the ZFACM algorithm.

Observing Fig. 4.17 the following remarks can be made. For all three algorithms the maximum value of the autocorrelation matching function occurs at the correct source location: 7.2 km and 31 m deep. All three results show a strong resemblance. The IFACM and KzFACM results show a reasonably good match with some sidelobes of medium-high magnitudes present in the search area. The ZFACM result is a moderate match where many sidelobes of high magnitudes occur. The peak-to-sidelobe ratio for this result is very small which makes the source localization difficult. For all three algorithms, the shown patterns are similar to the expected ray paths for a negative sound speed profile. The sidelobes mainly occur in the upper part of the water column where the rays will cross each other more. The IFACM and KzFACM footprints are the same in size and shape, while the ZFACM footprint is larger.

Comparing these results with the shallow array results of Case 1 (Figs. 4.1(b), 4.2(a) and 4.3(a)), the following can be observed. Although in each case the transient and the replica signals were 100% the same, an isospeed environment (Case 1) provides a better match for all three algorithms than a strong negative SSP environment (Case 3). The footprint sizes are approximately the same. However, in Case 3 many sidelobes of high magnitudes are present on the ambiguity surface. This difference can be explained as follows. First of all, note that the larger source range for Case 3 that could contribute to the higher sidelobes. Second, the downward refracting rays in Case 3 will reduce the number of multipath interceptions by an array compared to an isospeed environment with no ray bending. Less multipath interception will result in a worse match.

Regarding Fig. 4.18 the following observations can be made. Very high values of the autocorrelation matching function for all three algorithms occur at several different locations in the search area. Making an unrealistic adjustment in the dynamic range, setting the lower limit only 0.03 less than the maximum value, results in a good source location match for the IFACM and KzFACM

algorithms. However, for the ZFACM algorithm, this adjustment still results in too many sidelobes of high magnitudes in the search area. These outcomes are not shown in this report because of the unrealistic dynamic range adjustment. Since the numerous locations of sidelobes result in a failure to locate the actual source location, a discussion about the footprint sizes is not meaningful.

Comparing the results for the deep array with the shallow array results (Fig. 4.17), the following can be noted. Even without mismatch, for the deep array all algorithms fail to result in a reasonable match, where for the shallow array all three algorithms provide some match. A possible reason for this result is that the source could be located in a shadow zone.

The second situation for this case contains an environmental mismatch in the sound speed profile. The exact bottom profile and all other input parameters are known.

The sound speed profile mismatch only exists in the lower part of the water column. The sound speed profile of 1528 m/s at the surface and 1510 m/s at a depth of 50 m is exactly the same for both the actual and the assumed profile. The actual profile continues with a sound speed of 1489 m/s at a depth of 100 m, where the assumed profile continues with the initial sound speed profile gradient resulting in a sound speed of 1492 m/s at a depth of 100 m. Thus, the actual sound speed profile gradient is more negative (more downward refracting) over the second part of the water column than the assumed sound speed profile gradient.

Figure 4.19 shows the ambiguity surfaces of the three algorithms for the shallow array. Observing this figure the following remarks can be made. For all three algorithms the maximum value of the autocorrelation matching function occurs very close to the actual source location. The calculated source depth is for all three algorithms approximately 4.5 m deeper than the actual depth. The calculated source range for the IFACM algorithm is 80 m further than the actual

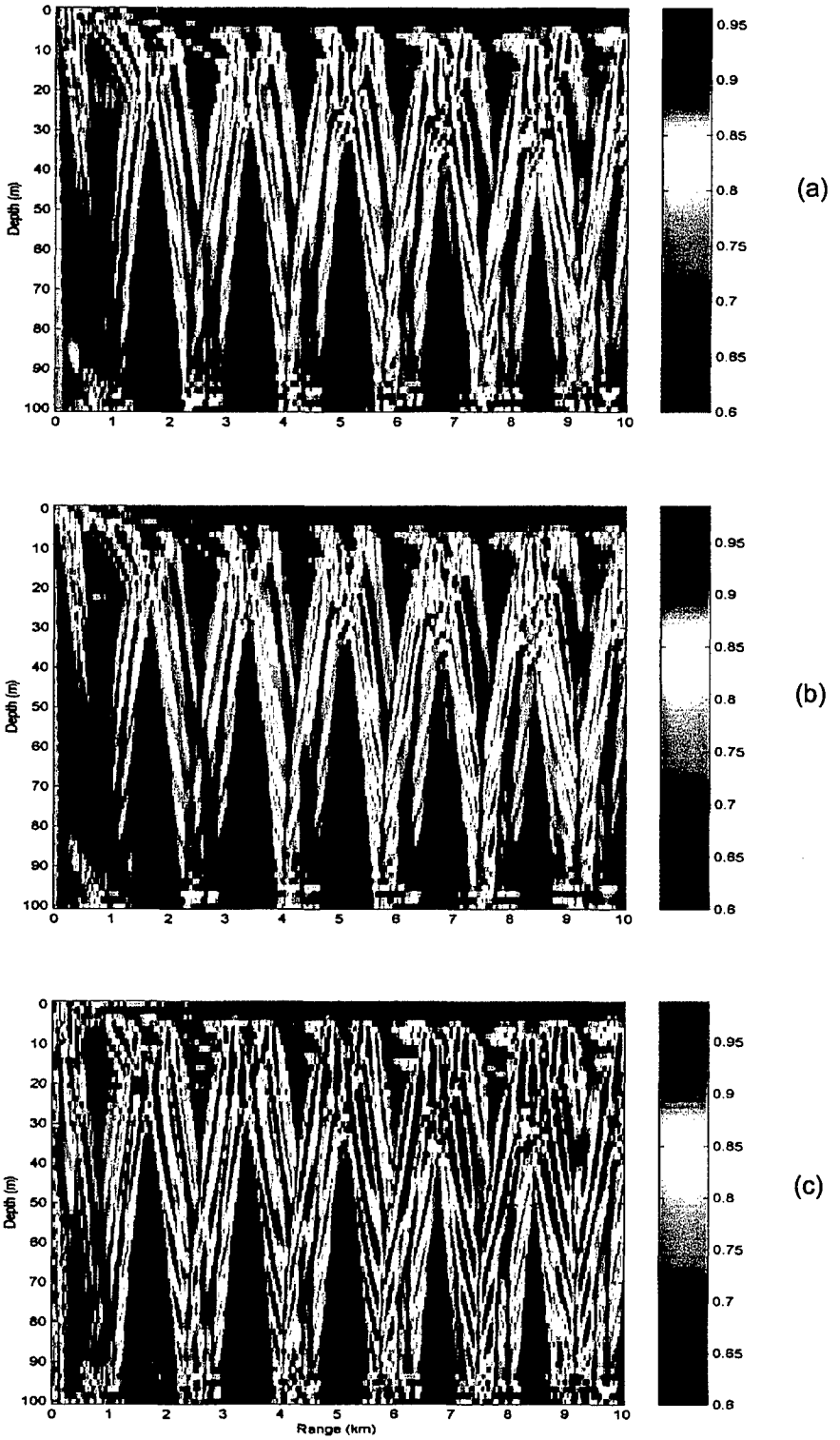

Figure 4.19: For Case 3, the ambiguity surfaces for the shallow array in a SSP mismatch situation: (a) the IFACM algorithm; (b) the KzFACM algorithm; (c) the ZFACM algorithm.

range. The other two algorithms calculated the exact actual range. Note that for exact location determination, larger views are used than shown in this report. The IFACM and KzFACM results show a good match, and the ZFACM result is a moderate match. The ZFACM ambiguity surface clearly has higher sidelobes than the other two surfaces. The peak-to-sidelobe ratio for ZFACM is less than that for the other two algorithms, which means difficult source localization. In all cases the footprints have a stretched shape in the direction of the ray paths. The footprint size for IFACM and KzFACM is equal in range, while KzFACM is larger in depth. ZFACM's footprint is largest in range and depth.

Comparing the shallow array results in a SSP mismatch situation with the shallow array results for Case 3 with no environmental mismatch (Fig. 4.17), the following can be noted. For both situations the ambiguity surfaces show patterns similar to the ray path patterns. The patterns are essentially the same with different amplitude levels. A mismatch in source depth appears in the SSP mismatch situation for all algorithms. The mismatch in source range as calculated only by the IFACM algorithm is unexpected and can not be explained at this stage. All three results show degradation in the SSP mismatch situation, where it also must be noted that this phenomenon is smallest for the KzFACM algorithm. In other words, it seems that KzFACM in this case is most robust for a SSP mismatch.

Figure 4.20 represents the ambiguity surfaces for the three algorithms for the deep array. Regarding this figure the following observations can be made. For all three algorithms the maximum value of the autocorrelation matching function occurs very close to the actual source location. The calculated source depth is for all three algorithms approximately 3 m shallower than the actual depth. The calculated source range matches the actual range for all three algorithms. Again, all three results show a close resemblance, where the sidelobes in the ZFACM results have higher values. The footprint sizes are

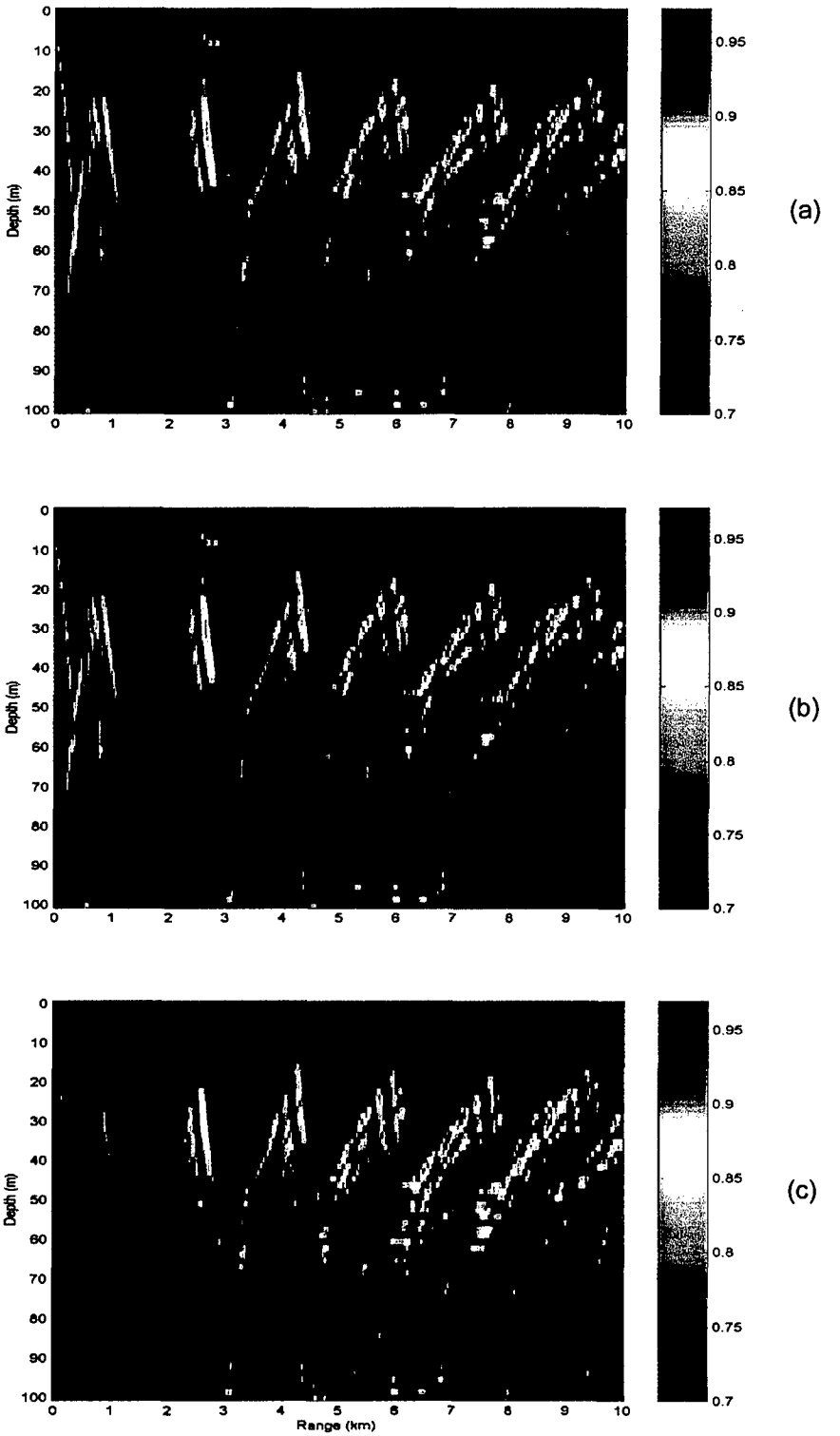

Figure 4.20: For Case 3, the ambiguity surfaces for the deep array in a SSP mismatch situation: (a) the IFACM algorithm; (b) the KzFACM algorithm; (c) the ZFACM algorithm.

small, and approximately equal for all three algorithms. Remarkable is the fact that the sidelobes in the search area mostly appear to be in the lower part of the upper half of the water column. At that depth, the mismatch in sound speed profiles has not yet been introduced. However, downward refracting rays at that depth have experienced most of the SSP mismatch from the deeper part of the water column.

Comparing the results with the shallow array results for the same SSP mismatch situation (Fig. 4.19), the following can be noted. The different array depths lead to different mismatches in the source depth. The shallow array algorithm results calculate the source depth 4.5 m deeper than the actual source depth. The deep array algorithm results calculate the source depth 3 m shallower than the actual source depth. The deep array results show fewer sidelobes in the ambiguity surface, as well as smaller footprints for all three algorithms. Based on these observations it seems that with a SSP mismatch situation, the algorithms applied with the deep array performs better than with the shallow array. For both arrays their order of success is KzFACM, IFACM and ZFACM. The better results of the deep array can be explained as follows. For a negative sound speed gradient, meaning downward refracting rays, the deep array will intercept more multipaths than the shallow array. Although the deep array is closer to the mismatch region than the shallow array, apparently the interception of more multipaths by the deep array results in a better match.

Comparing the deep array results for the SSP mismatch situation with the deep array results without environmental mismatch (Fig. 4.18), the following can be observed. The SSP mismatch situation results give a better match of the actual source location than without mismatch. Although the source location has a small depth mismatch for the SSP mismatch situation, the maximum in the ambiguity surface appears in the vicinity of the actual source location. Without mismatch, many sidelobes of high magnitudes are present, and none of them is really close to the actual source location. The reason for the considerable improvement in performance with the SSP mismatch is unclear, however.

The last situation for Case 3 contains an environmental mismatch in the bottom bathymetry. The sound speed profile and all other input parameters are known. The bottom bathymetry mismatch is an assumed flat bottom at a depth of 100 m versus the actual bottom. Figures 4.21 and 4.22 show the ambiguity surfaces for the three algorithms for the shallow array and the deep array, respectively.

Regarding Fig. 4.21 the following observations can be made. For all three algorithms the maximum value of the autocorrelation matching function occurs somewhat near the actual source location. The actual source range of 7.2 km is calculated 80 m further, the actual source depth of 31 m is calculated 3 m deeper. Besides that, all three results show a familiar pattern similar to the ray path pattern for a negative sound speed profile. The displayed matches are fairly good. The IFACM and KzFACM perform best, showing only striping of medium magnitudes through the search area. The ZFACM result is slightly worse. The striping in the search area is of higher magnitudes. Footprint sizes are small for all three algorithms.

Comparing the shallow array results for a bottom bathymetry mismatch with the shallow array results for Case 3 with no environmental mismatch (Fig. 4.17), the following can be noted. For both situations the ambiguity surfaces show patterns similar to the ray path patterns. A mismatch in source location appears in the bottom bathymetry mismatch situation for all algorithms, as observed in Case 2 with bottom bathymetry mismatch. All three results show a better match with bottom bathymetry mismatch, especially the ZFACM result. Also note that the footprint sizes are smaller in range with the bottom bathymetry mismatch situation.

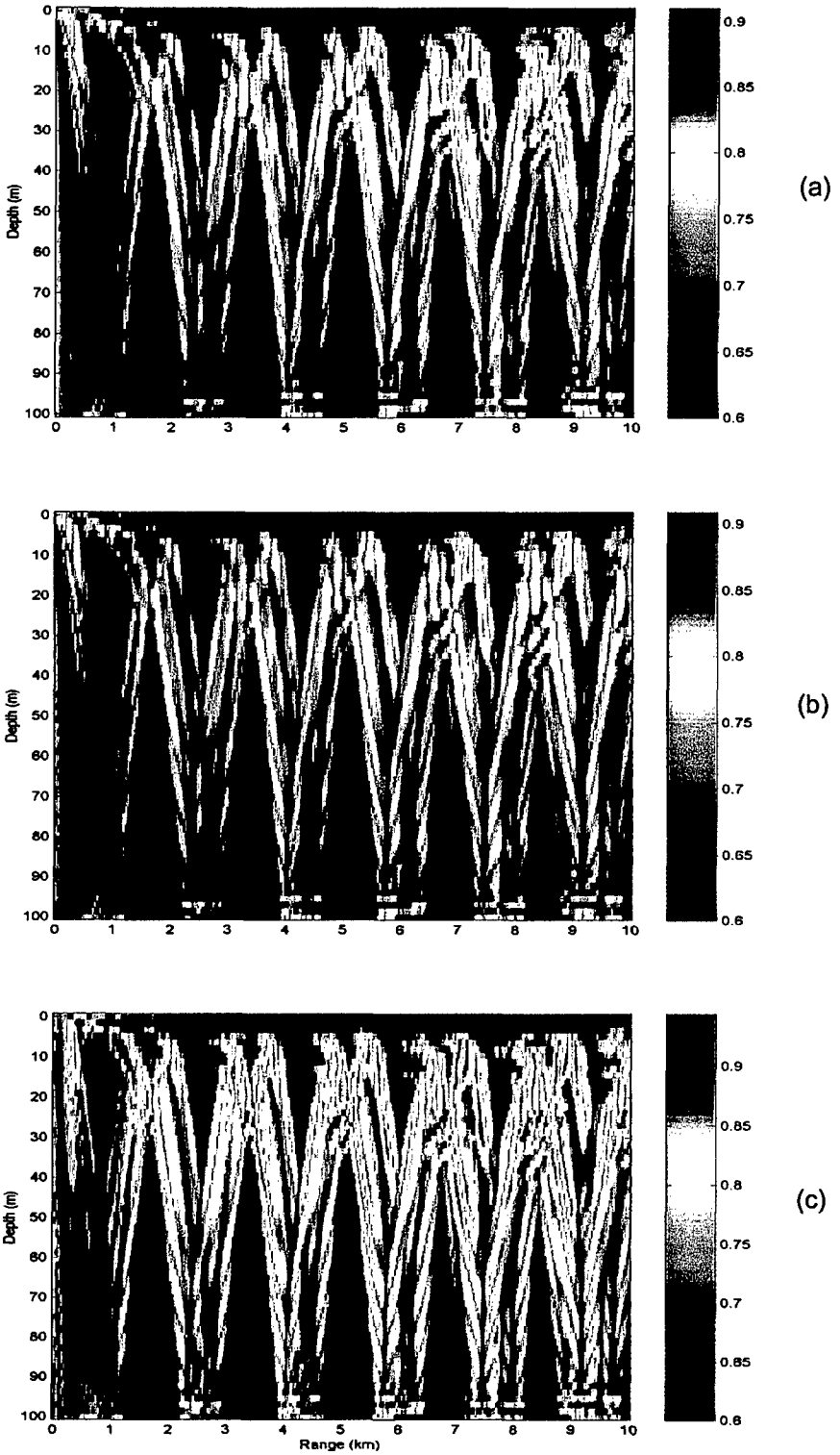

Figure 4.21: For Case 3, the ambiguity surfaces for the shallow array in a bottom bathymetry mismatch situation: (a) the IFACM algorithm; (b) the KzFACM algorithm; (c) the ZFACM algorithm.

Observing Fig. 4.22 the following remarks can be made. For the shown dynamic range for all three algorithms, the maximum value of the autocorrelation matching function does not occur at the actual source location. The calculated source depth is for all three algorithms approximately 1.5 m deeper than the actual depth. The calculated source range matches the actual range for all three algorithms. Note that in order to determine exactly the calculated source location from the information in Fig. 4.22, an adjusted dynamic range must be used. The adjustment meant changing the lower limit to 0.95. This is probably an unrealistic dynamic range adjustment and therefore these ambiguity surfaces are not shown here. All three algorithms show a moderate match with many sidelobes of medium-high magnitudes present on the ambiguity surfaces. Remarkable is that for this situation the ZFACM result shows the fewest sidelobes. The KzFACM result shows a better match than the IFACM result. The footprint sizes are approximately the same for all three algorithms.

Comparing these deep array results with the shallow array results for the same mismatch situation (Fig. 4.21), the following can be noted. Both arrays have a source depth mismatch. The shallow array has a mismatch of 3 m (deeper), the deep array results have a mismatch of 1.5 m (deeper). The deep array results have no mismatch in range. The shallow array results have a range mismatch of 80 m (further). The shallow array results show less sidelobes on the ambiguity surface, as well as smaller footprints for all three algorithms. Based on these observations it seems that with a bottom bathymetry mismatch, the algorithms applied with the deep array perform better than with the shallow array. For both arrays their order of success is KzFACM, IFACM and ZFACM. Again, it seems that more multipath interceptions, even with introduced mismatch, give better results than those with fewer interceptions.

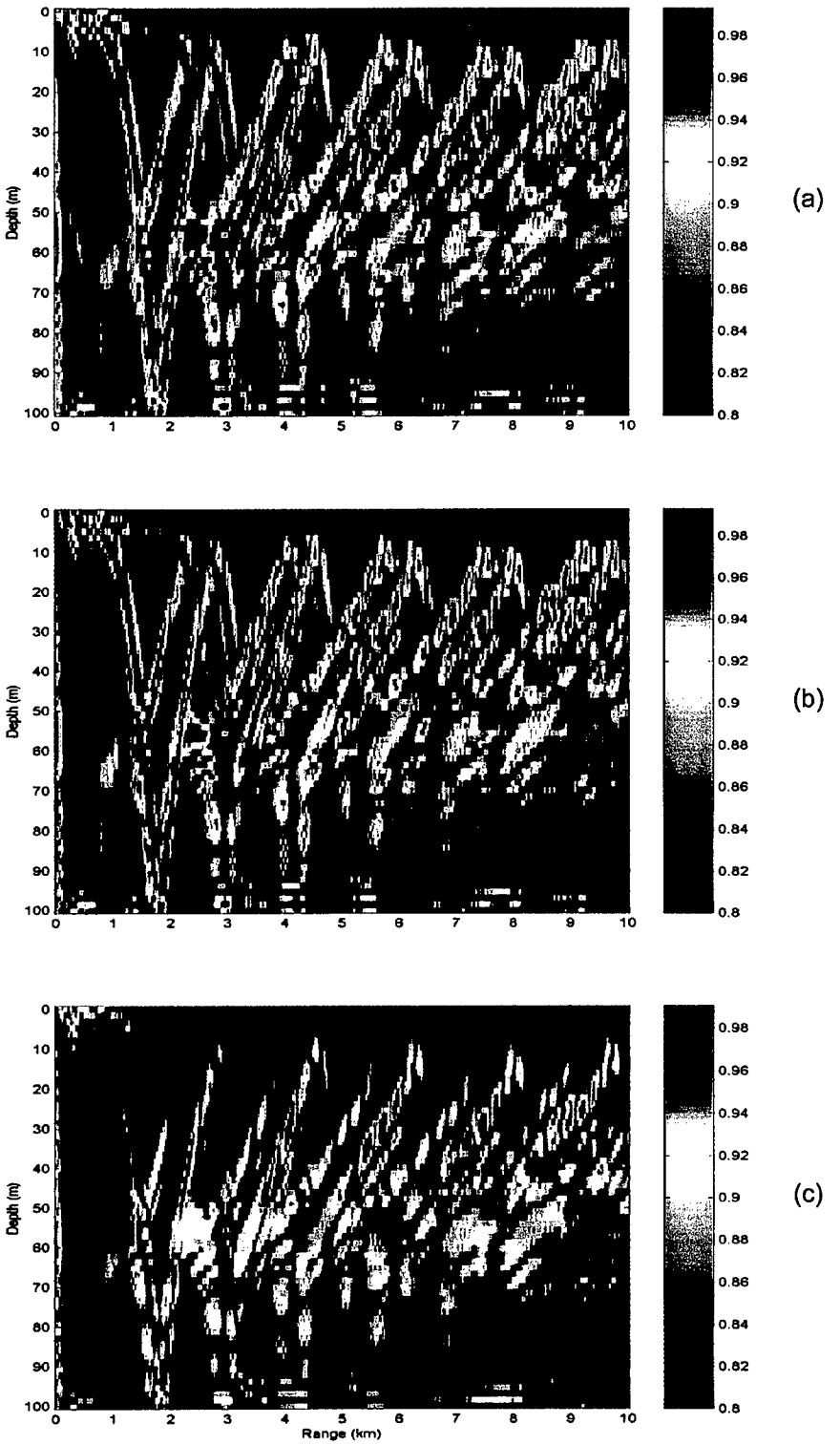

Figure 4.22: For Case 3, the ambiguity surfaces for the deep array in a bottom bathymetry mismatch situation: (a) the IFACM algorithm; (b) the KzFACM algorithm; (c) the ZFACM algorithm.

Comparing the deep array results with the bottom bathymetry mismatch and the deep array results without environmental mismatch (Fig. 4.18), the following can be observed. The bottom bathymetry mismatch situation results give a better match of the actual source location than without mismatch. Although the source location has a small depth mismatch for the bottom bathymetry mismatch situation, the maximum in the ambiguity surface appears in the vicinity of the actual source location. Without environmental mismatch, many sidelobes with high magnitudes are present scattered over most of the ambiguity surface.

D. SUMMARY OF FINDINGS

The previous three sections have shown many different results for the three algorithms. The algorithms have been tested over two different array depths and three different environmental cases, of which for two cases mismatch situations have been introduced. In total 42 different ambiguity surfaces have been presented and discussed. In order to gain more insight in relative performance of the algorithms the abbreviated results are tabulated (Tables 4.1, 4.2 and 4.3) in a summarizing fashion. Since the previous sections contained the detail comments, this section will summarize only overall remarks on findings that appeared in all three environments.

Results from earlier thesis work had shown that the FACM algorithm performs better than the TACM algorithm. As explained in the last two paragraphs in Chapter II, this suggests that the matching of the squared amplitudes of the signals in the time-domain give better results than in the frequency-domain. In this thesis, it has been shown that the driving factor of a successful autocorrelation matching algorithm is the time-domain component. This conclusion is based upon the fact that the developed algorithms for this

thesis in most occasions showed a close resemblance. The sidelobes occurred at the same locations and the differences between the algorithms were essentially sidelobe magnitudes and peak-to-sidelobe ratios. Also, it has been shown that, although at a much smaller scale, the KzFACM algorithm performs better than the ZFACM algorithm in most cases. This implies that the matching of the squared amplitudes of the signals in the depth- and time-domain give better results than in the wavenumber- and time-domain.

	IFACM	KzFACM	ZFACM
Case 1 Isospeed SSP, Shallow array, No mismatch	Source location matched Few sidelobes (max 80%) Footprint: 80 x 3 m	Source location matched Few sidelobes (max 80%) Footprint: 80 x 3 m	Source location matched Some sidelobes (max 89%) Footprint: 120 x 6 m
Case 1 Isospeed SSP, Deep array, No mismatch	Source location matched No sidelobes Footprint: 80 x 3 m	Source location matched No sidelobes Footprint: 80 x 3 m	Source location matched One sidelobe (max 62%) Footprint: 80 x 4.5 m

Table 4.1: The summarized results for the IFACM, KzFACM and ZFACM algorithms in the Case 1 environment.

The fact that a better match was sometimes achieved with than without environmental mismatch was initially surprising. Later thoughts on this phenomenon led to the following explanation. When no mismatch has been introduced, the source data and the replica data are ideally 100% equal. Furthermore, the propagation can have similar structure at other locations in the waveguide. Matching these similar data sets can lead to many high value correlations that will appear as sidelobes of high magnitudes. In an ambiguity surface with these high magnitude sidelobes, the actual source location may easily be disguised. When the mismatch has been introduced, the source data and the replica data can be very different for most of the search area, except

	IFACM	KzFACM	ZFACM
Case 2 Positive SSP, Shallow array, No mismatch	Source location matched Few 'shadows' (max 88%) Footprint: 80 x 6 m	Source location matched Few 'shadows' (max 88%) Footprint: 80 x 6 m	Source location matched Some 'shadows' (max 93%) Footprint: 80 x 9 m
Case 2 Positive SSP, Deep array, No mismatch	Source location matched One sidelobe (max 85%) Footprint: 40 x 3 m	Source location matched One sidelobe (max 85%) Footprint: 40 x 6 m	Source location matched One sidelobe (max 85%) Footprint: 40 x 6 m
Case 2 Positive SSP, Shallow array, SSP mismatch	Source location mismatch (40 m closer x 1.5 m shallower) One sidelobe (max 92%) Footprint: 80 x 3 m	Source location mismatch (40 m closer x 1.5 m shallower) One sidelobe (max 90%) Footprint: 80 x 3 m	Source location mismatch (40 m closer x 1.5 m shallower) Some sidelobes (max 96%) Footprint: 160 x 3 m
Case 2 Positive SSP, Deep array, SSP mismatch	No source location match (very large range mismatch) Many sidelobes (max 98%) Footprint: n.a.	No source location match (very large range mismatch) Many sidelobes (max 98%) Footprint: n.a.	No source location match (very large range mismatch) Many sidelobes (max 98%) Footprint: n.a.
Case 2 Positive SSP, Shallow array, Bathymetry mismatch	Source location mismatch (120 m further) Many 'shadows' (max 91%) Footprint: 360 x 6 m	Source location mismatch (120 m further) Many 'shadows' (max 91%) Footprint: 360 x 6 m	Source location mismatch (120 m further) Many 'shadows' (max 91%), some sidelobes (max 88%) Footprint: 360 x 12 m
Case 2 Positive SSP, Deep array, Bathymetry mismatch	Source location mismatch (120 m further) No sidelobes Footprint: 40 x 3 m	Source location mismatch (120 m further) No sidelobes Footprint:40 x 3 m	Source location mismatch (120 m further) No sidelobes Footprint: 40 x 3 m

Table 4.2: The summarized results for the IFACM, KzFACM and ZFACM algorithms in the Case 2 environment, and its mismatch situations.

near the source location. A source location mismatch may be anticipated in the presence of bottom bathymetry mismatch (D'Spain, 1999). However, due to the overall difference between the source data and the replica data, any appearing

sidelobes may be smaller in magnitude than the calculated source location. Therefore, the resulting ambiguity surface with mismatch can display a better result than without mismatch.

In this thesis no ambiguity surfaces of the FACM algorithm for a single hydrophone are displayed. However, the input files for the IFACM algorithm are essentially these single hydrophone results. Therefore, the author claims to have seen a large number of FACM ambiguity surfaces and can comment on the single hydrophone results versus the IFACM results. It turns out that the hydrophone depth has a large impact on the success of the FACM algorithm. Within the span of a vertical line array, the autocorrelation matching results between, for example, hydrophone one, eight and sixteen can differ significantly. The IFACM algorithm is basically an average over the 16 single hydrophone results. Therefore, the statement that multiple hydrophone algorithms give better results is valid. However, the possibility of a better result with a single hydrophone located at exactly the optimum depth should be mentioned as well.

The different algorithms have different runtimes. The KzFACM algorithm takes about five hours and the ZFACM algorithm takes about two hours to calculate and display their ambiguity surface. The IFACM algorithm takes less than five minutes to calculate and display its ambiguity surface, once the single hydrophone FACM results have been computed. These calculations take approximately one hour per hydrophone. If these calculations could be done for all hydrophones simultaneously, the total runtime for the IFACM algorithm would be just over one hour. In that case, the IFACM algorithm would be twice as fast as the ZFACM algorithm and five times as fast as the KzFACM algorithm. Since for most cases the IFACM and the KzFACM results show a close resemblance, the runtime difference can become an important argument in a more operational environment.

	IFACM	KzFACM	ZFACM
Case 3 Negative SSP, Shallow array, No mismatch	Source location matched Some striping (max 85%) Footprint: 80 x 7.5 m	Source location matched Some striping (max 85%) Footprint: 80 x 7.5 m	Source location matched More striping (max 92%) Footprint: 120 x 9 m
Case 3 Negative SSP, Deep array, No mismatch	No source location match Much striping (max 98%) Footprint: n.a.	No source location match Much striping (max 98%) Footprint: n.a.	No source location match Much striping (max 94%) Footprint: n.a.
Case 3 Negative SSP, Shallow array, SSP mismatch	Source location mismatch (80 m further x 4.5 m deeper) Mod. striping (max 89%) Footprint: 80 x 9 m	Source location mismatch (4.5 m deeper) Mod. striping (max 90%) Footprint: 80 x 15 m	Source location mismatch (4.5 m deeper) Much striping (max 96%) Footprint: 120 x 15 m
Case 3 Negative SSP, Deep array, SSP mismatch	Source location mismatch (3 m shallower) Little striping (max 90%) Footprint: 80 x 3 m	Source location mismatch (3 m shallower) Little striping (max 90%) Footprint: 80 x 3 m	Source location mismatch (3 m shallower) Some striping (max 91%) Footprint: 80 x 3 m
Case 3 Negative SSP, Shallow array, Bathymetry mismatch	Source location mismatch (80 m further x 3 m deeper) Some striping (max 87%) Footprint: 80 x 6 m	Source location mismatch (80 m further x 3 m deeper) Little striping (max 87%) Footprint: 80 x 6 m	Source location mismatch (80 m further x 3 m deeper) More striping (max 90%) Footprint: 80 x 6 m
Case 3 Negative SSP, Deep array, Bathymetry mismatch	Source location mismatch (1.5 m deeper) Much striping (max 96%) Footprint: 120 x 7.5 m	Source location mismatch (1.5 m deeper) Much striping (max 96%) Footprint: 120 x 7.5 m	Source location mismatch (1.5 m deeper) Some striping (max 94%) Footprint: 120 x 7.5 m

Table 4.3: The summarized results for the IFACM, KzFACM and ZFACM algorithms in the Case 3 environment, and its mismatch situations.

THIS PAGE INTENTIONALLY LEFT BLANK

V. CONCLUSIONS AND FUTURE WORK

A. CONCLUSIONS

In this thesis, several algorithms are developed to localize a broadband transient-like point source with a vertical line array. The algorithms are an adaptation of a previously developed frequency-domain autocorrelation matching (FACM) algorithm, based on matched field processing principles. The FACM algorithm was used to localize a transient with a single hydrophone. Its performance has been evaluated under environmental mismatch situations, and was determined to be the most successful algorithm compared to other similar algorithms. For this thesis, the newly developed algorithms have incorporated the additional information from the multiple elements in the array and adapted the FACM algorithm. The algorithms are depth- and frequency-domain autocorrelation matching (ZFACM), wavenumber- and frequency-domain autocorrelation matching (KzFACM), and the incoherent summation of the single element FACM results (IFACM). These algorithms have been evaluated for various different environmental situations and mismatches.

For many of the evaluated situations it turned out that all three algorithms produce similar results. This was the case for good matches, but also for less successful results. Since the only difference between the algorithms was in the treatment of the multiple element information, it is concluded that mainly the time-component of the matching envelopes is responsible for the general structure of the ambiguity surfaces. The additional wavenumber- or depth-component, completing the matching envelopes of the new algorithms, merely 'details' the final results in amplitudes and peak-to-sidelobe ratios. In this 'detailing' region the KzFACM algorithm generally produced a slightly better match than the ZFACM algorithm. The IFACM results were surprisingly similar to the KzFACM

results. In all cases, the results suggested that the use of the additional information from multiple elements does improve the accuracy and robustness of the localizations.

Also noticeable was the difference in calculation times. The IFACM algorithm was twice as fast as the ZFACM algorithm and five times as fast as KzFACM algorithm. This significant difference can be of operational importance, especially if the results are very similar.

For a slightly advanced environment, it was observed that in some cases the results appeared to be better with than without an introduced mismatch. A possible explanation for this phenomenon is the fact that, when no mismatch is introduced, the matching envelopes have almost the same values. This results in an ambiguity surface with many high-valued sidelobes, disguising the actual source location. Introducing a mismatch results in matching envelopes that are more distinct, except at the source location. This produces an ambiguity surface with only a small source location mismatch and low-valued sidelobes.

The following observations show that the placement of the source and the receiver within the environment, and the environment itself, have a large impact on the performance of the algorithms. One observation is that there were significant differences in the ambiguity surfaces computed using the single hydrophone FACM algorithm over the length of the array. Although these results were not shown in this report, it was clear that the combined use of array data with the algorithms developed here improved the peak-to-sidelobe ratios for the localization results. Another observation is that for upward refracting rays, the shallow array gave better results than the deep array. For downward refracting rays the deep array was generally more successful. The number of multipath interceptions is the driving factor for this success. In mismatch situations, more stable multipath interceptions give a better result. However, if the receiving array intercepts a large number of multipaths pertubated by the environmental mismatch, the results presumably degrade. This brings up the third observation which is that in two occasions the deep array was not successful at all. For both

cases the rays were either upward or downward bending, causing shadow zones at certain locations in the search area. Probably for these two cases, the source-array geometry is such that a shadow zone is involved, causing the complete mismatch.

B. RECOMMENDATIONS FOR FUTURE WORK

Applying the developed algorithms to real data seems to be the most logical and interesting follow-on. With the possibilities of the MMPE model the real life scenario could be simulated as well, and results of both real data and synthetic data could be compared.

Another path for future work could be a continuation of the simulation runs with the algorithms for a more realistic environment. After this environment has been established, the sensitivity of the algorithms for (other) environmental mismatches can be explored further.

THIS PAGE INTENTIONALLY LEFT BLANK

LIST OF REFERENCES

Brune, J., "Transient Localization in Shallow Water Environments," Master's Thesis, Naval Postgraduate School, March 1998.

Correa, A.F. Bettega, "Shallow Water Acoustic Variability and Influences on Autocorrelation Matching Localization Algorithms," Master's Thesis, Naval Postgraduate School, December 1998.

D'Spain, G.L., Murray, J.J., Hodgkiss, W.S., Booth, N.O. and Schey, P.W., "Mirages in shallow water matched field processing," J. Acoust. Soc. Am. 105 (6), 3245-3265 (1999).

Hardin, R.H., and Tappert, F.D., "Applications of the split-step Fourier method to the numerical solution of nonlinear and variable coefficient wave equations," SIAM Rev.15, p. 423, 1973.

Jensen, F.B., Kuperman, W.A., Porter, M.B., and Schmidt, H., *Computational Ocean Acoustics*, American Institute of Physics Press, Woodbury, NY, 1994.

Kinsler, L.E., Frey, A.R., Coppens, A.B., Sanders, J.V., *Fundamentals of Acoustics*, John Wiley and Sons, Inc., New York, NY, 1982.

de Kooter, P.M., "Variations on Autocorrelation Matching and the SIFT Localization Algorithm," Master's Thesis, Naval Postgraduate School, March 1997.

Miller,J.H., Benson, J.L., Chiu, C.-S, and Smith, K.B., "Transient Localization project at NPS," Technical Report NPS-UW-96-001PR, Naval Postgraduate School, April 1996.

Smith, K.B., Personal communication, Naval Postgraduate School, January 1999. The Monterey-Miami Parabolic Equation (MMPE) model is an upgraded version of the University of Miami Parabolic Equation (UMPE) model (Smith and Tappert, 1993).

Smith, K.B., and Tappert, F.D., "UMPE: The University of Miami Parabolic Equation Model, Version 1.0," Marine Physical Labortory Technical Memo 432, 1993.

Tappert, F.D., "The parabolic approximation method," in *Lecture Notes in Physics,* Vol.70, Wave Propagation and Underwater Acoustics, edited by J.B Keller and J.S. Papadakis, Springer Verlag, New York, NY, 1977.

Thomson, D.J., and Chapman, N.R., "A wide-angle split step algorithm for the parabolic equation models," *JASA Suppl.* 1 83, 1983.

Tolstoy, A., *Matched Field Processing For Underwater Acoustics,* World Scientific, River Edge, NJ, 1993.

INITIAL DISTRIBUTION LIST

1. Defense Technical Information Center 2
   8725 John J. Kingman Road, STE 0944
   Ft. Belvoir, VA 22060-6218

2. Dudley Knox Library 2
   Naval Postgraduate School
   411 Dyer Road
   Monterey, CA 93943-5101

3. Engineering & Technology Curricular Office 1
   Naval Postgraduate School, Code 34
   411 Dyer Road
   Monterey, CA 93943

4. Prof. Kevin B. Smith 3
   Department of Physics, Code PH/Sk
   Naval Postgraduate School
   Monterey, CA 93943-5117

5. Mitchell Shipley, CDR US Navy 1
   Department of Physics, Code PH/Sm
   Naval Postgraduate School
   Monterey, CA 93943-5117

6. Ministry of Defense 1
   Directorate Material Royal Netherlands Navy
   Department of Weapon and Communication Systems
   OSAO, Wetenschappelijk Medewerker
   Postbus 20702
   2500 ES 's Gravenhage
   The Netherlands

7. Flagofficer Royal Netherlands Naval College 1
   Attn: ir J.A.J. Biemond
   Postbus 10000
   1780 AC Den Helder
   The Netherlands

8. G.Tas 1
Witte de Withstraat 55
3342 TV Hendrik Ido Ambacht
The Netherlands

9. J.L. Spoelstra, RADM RNethNavy (ret) 1
Director Saclant Undersea Research Centre
La Spezia
Italy
APO AE 0913-5000

10. G.Tas, LCDR RNethNavy 2
Vogelzand 3310
1788 MD Den Helder
The Netherlands